International Symposium on Qualification of dynamic analyses of dams and their equipment and of probabilistic assessment of seismic hazard in Europe, 31th August – 2nd September, Saint-Malo, France (this symposium) (eds. Fry, J.-J. and Matsumoto, N.)

Soil properties and seismic stability of old and new Fujinuma dams

F. Tatsuoka
Tokyo University of Science, Japan

T. Tanaka
Japan Association of Rural Solutions for Environmental Conservation and Resource Recycling, Japan

K. Ueno
National Institute for rural Engineering, Japan

A. Duttine
Integrated Geotechnology Institute, Japan

Y. Mohri
Ibaraki University, Japan

ABSTRACT: The collapse of the main and auxiliary Fujinuma dams by the 2011 Great East Japan Earthquake and its restoration to much more stable ones, to be completed by April 2017, are described. The soil types and compacted dry densities of the collapsed old dams and those of the new dams obtained at the design stage are reported. The results from a series of monotonic undrained triaxial tests before and after cyclic undrained loading of saturated specimens of the materials from the old dams and those to be used to construct the new dams compacted to different dry densities are summarized to simulate the collapse of the old dams by the Newmark-D method and the pseudo-static non-linear FEM. The analyses take into account the seismic forces and the continuous degradation of the stress-strain properties by cyclic undrained loading. It is shown that the old dams collapsed due mainly to that: 1) the compacted state was generally poor; 2) the top fill consisted of particularly poor compacted sandy soil, which would have resulted in a significant reduction of undrained strength by cyclic loading and fast erosion; and 3) prolonged strong seismic motion. It is shown that the collapse of the old main dam is simulated very well by the proposed analysis methods and the new dam is much more stable by better compacting better soil types.

1 INTRODUCTION

Fujinuma agricultural irrigation reservoir was located on the right branch of upper Sunoko Rive in Sukagawa city, Fukushima Prefecture and had main and auxiliary dams (Figs. 1 &2). The construction of these dams was started April 1937, suspended during World War II and completed October 1949. The main dam was an earth-fill dam with a height of 18.5 m and the crest length of 133.2 m (Fig. 3). The auxiliary dam was also an earth-fill dam with a height of 10.5 m and a crest length of 72.5 m (Table 1). During a period from 1977 to 1979, the spillway and surface protection work of the main dam were repaired and, for a period from 1984 to 1992, counter measures against leakage by grouting was constructed and upgrading of intakes was conducted. The agricultural water taken from Fujinuma Reservoir irrigates the land of 837 ha and the dam had been managed and operated by Ebanagawa Irrigation District.

Both main and auxiliary dams totally collapsed by the 2011 Tohoku Region Pacific Coast Earthquake (i.e. the 2011 Great East Japan Earthquake) (M= 9.0), which took place 14:46. As indicated by a broken curve in Figure 2b, a large amount of released water caused by the breach of the main dam reached the downstream community causing a loss of seven lives and one missing. By the earthquake, some 750 of other small irrigation dams were damaged in the Fukushima Prefecture only. Fukushima Prefecture set up a panel to evaluate the seismic stability of irrigation dams and small ponds for agricultural purpose and to investigate the cause of collapse of the Fujinuma dams. The panel consisted of the second author of this paper (chair) and the first and last authors (members). The first panel meeting was held on August 4 and 5 and in total five meetings were held until 25 January 2012. An outline of the report of the panel was reported by Tanaka et al. (2012). It is reported that the old dam collapsed due mainly to that: 1) the compacted state of the whole dam was generally poor; 2) the top fill consisted of particularly poor compacted sandy soil, which is highly susceptible to a significant reduction of undrained strength when subjected to cyclic undrained loading while highly erodible when subjected to over-topping flow; and 3) the seismic motion was strong and prolonged. Following this panel, another advisory panel was organized consisting of the same three members as the above for the restoration of the collapsed dams to new ones that are much more stable than the old ones. At the time of writing this report (August 2016), the new dams are under construction to be completed by April 2017.

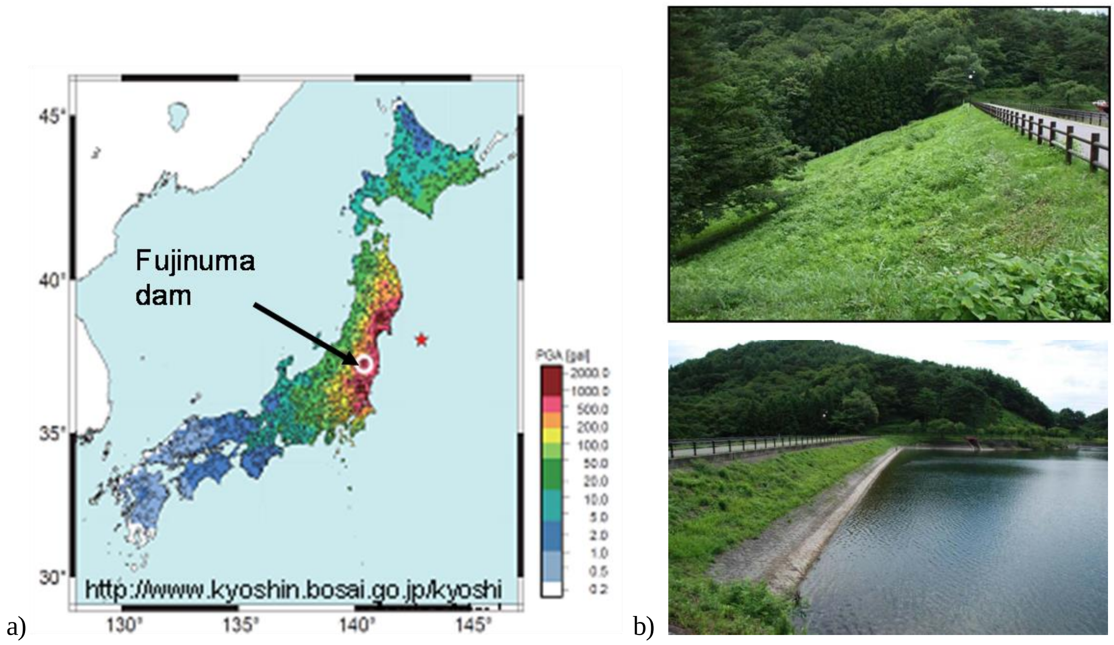

Figure 1. a) Seismic intensity distribution of the 2011 Great East Japan Earthquake; and the location of Fujinuma dam; and views of the old Fujinuma dam (Tanaka etal. 2012).

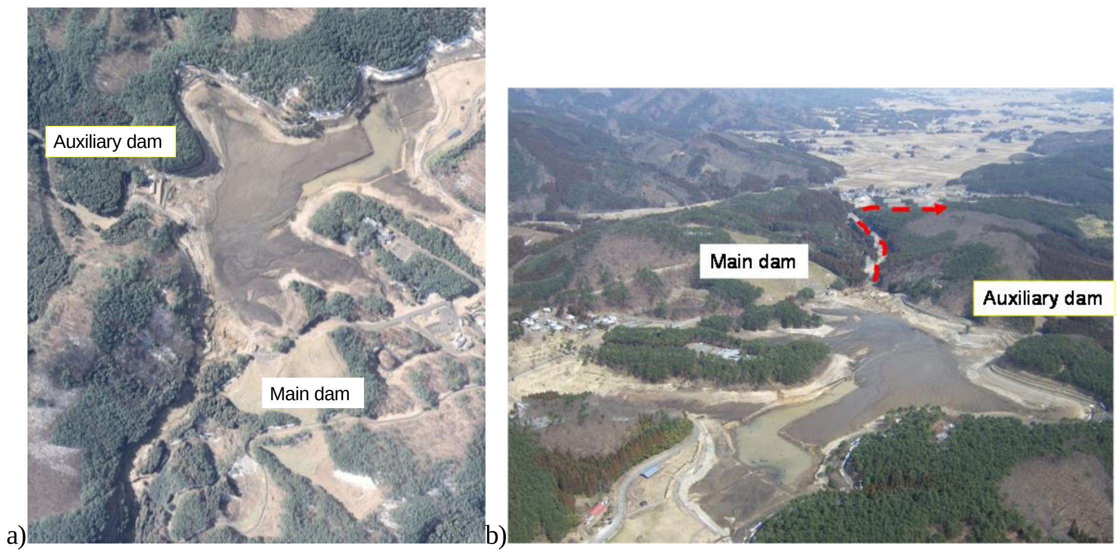

Figure 2. Aerial pictures taken after collapse, Fujinuma Dam (Tanaka et al. 2012).

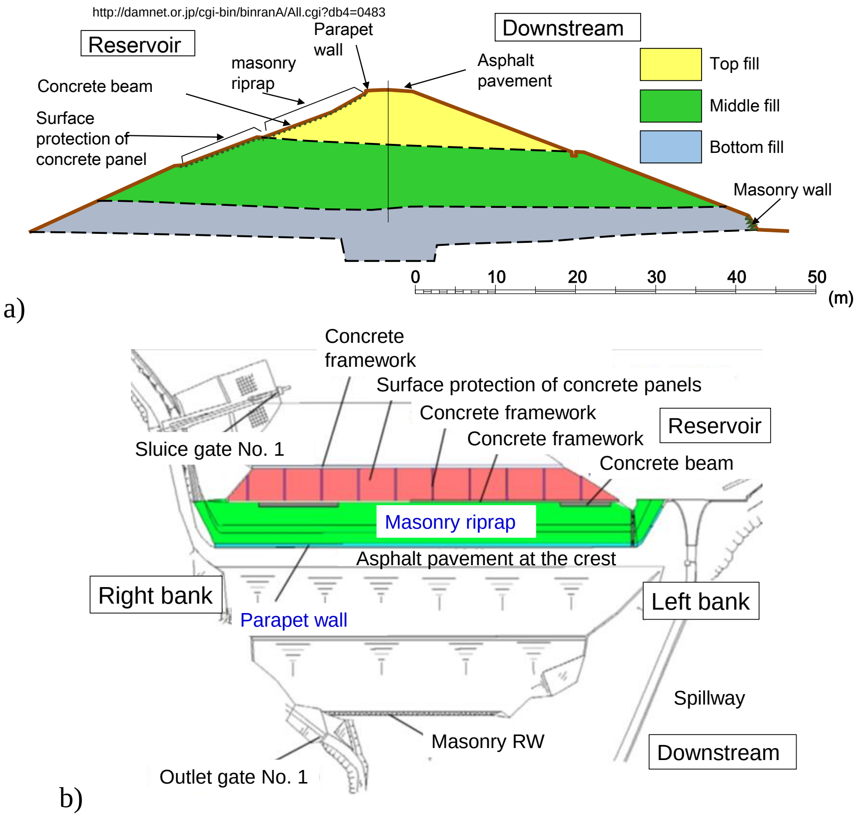

Figure 3. a) Typical cross-section; and plan of main Fujinuma dam (Tanaka etal. 2012).

Table 1. Outline of old Fujinuma dams.

Commissioning Entity	Fukushima Prefecture
Location	Sukagawa City, Fukushima Prefecture
Purpose	Irrigation
Type	Main dam: earth-fill dam Auxiliary dam: earth-fill Dam
Height	Main : 18.5 m Auxiliary : 10.5 m
Crest length	Main : 133.2 m Auxiliary : 72.5 m
Volume	Main : 99,000 m^3
Total storage capacity	1,500,000 m^3
Effective storage capacity	1,480,000 m^3
Completed	1949

In this report, the soil types and estimated compacted states in the collapsed dams, the results from a series of monotonic undrained loading triaxial tests performed before and after the application of cyclic undrained loading causing different strains (as explained in Tatsuoka 2016) on saturated specimens of the materials retrieved from the site compacted to different dry densities are summarized. Then, the results of "slip displacement analysis by the Newmark-D method" and "residual deformation analysis by the pseudo-static non-linear FEM", both taking into the seismic forces and the continuous degradation of the stress-strain properties by cyclic undrained loading" (as explained in Duttine et al. 2016), of the old dams are reported. Similar data of better backfill materials compacted better obtained at the design stage of the new dams are also summarized. It is shown that it is difficult to predict this collapse when based on the conventional design procedure for irrigation earth-fill dams in Japan, while the new simplified method can capture the collapse mechanism of the old dams. It is also shown that this method is useful for the design of the new dams by showing that the new dams will be highly stable even when subjected to the same earthquake motion by which the old dams collapsed.

2 COLLAPSE OF FUJINUMA DAMS AND THEIR RESTORATION

2.1 *Collapse by the 2011 Great East Japan Earthquake*

Figure 4a shows the picture of the breaching state of the old main dam. The picture was taken around PM 15:11, 11 March 2011, while the main shock of the earthquake started 14:46. Therefore, it is very likely that the start of collapse was during the earthquake. Figure 4b shows the dam after full collapse. Referring to the inside structure of the dam shown in Figure 4c, the fact that part of the upstream side of the middle fill survived while the top fill was totally lost suggests that the soil type of the top fill is much more erodible than the second fill (as substantiated by a soil investigation performed after the earthquake, as described below). The zone where the embankment was highest and the previous stream was running was eroded most deeply.

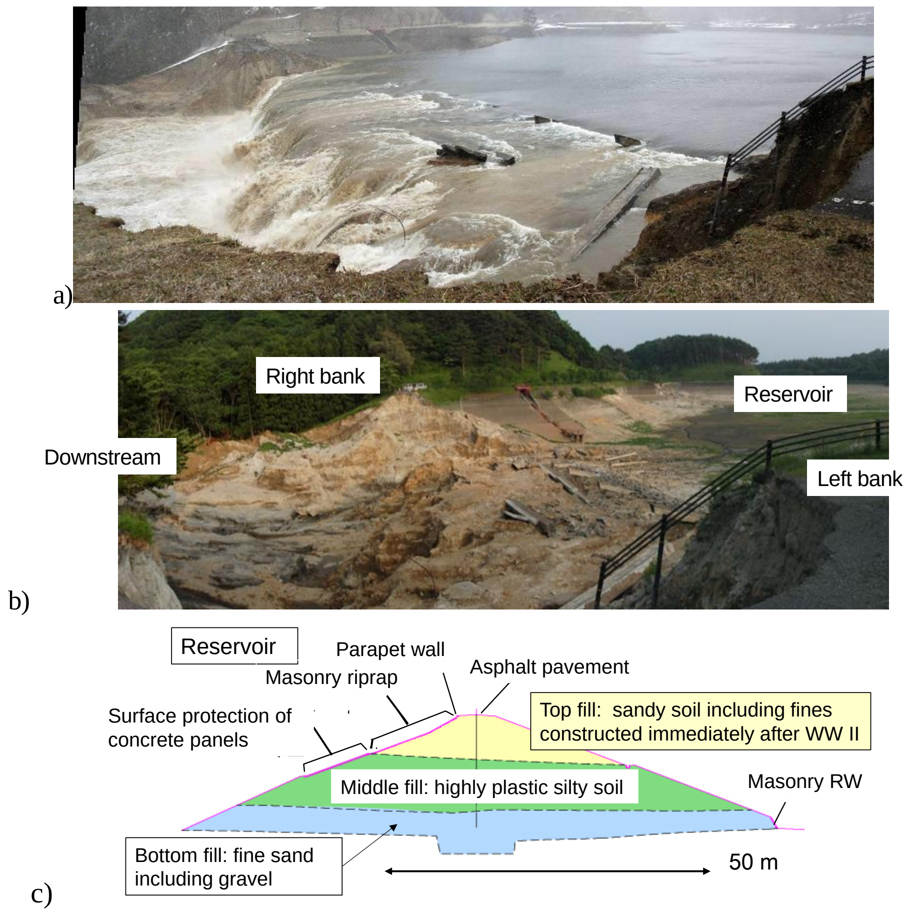

Figure 4. a) Breaching state of Fujinuma main dam (taken around PM 15:11, 11 March 2011; by the courtesy of Fukushima Prefecture) (Tanaka et al. 2012); b) after full collapse (by the courtesy of Dr. Hori, T.); and c) internal structure.

Figure 5a shows the inferred failure mechanism of the old main dam. The numbers indicated in this figure indicate the sequence of occurrence. It was inferred that firstly slide 1 took place in the top fill. Despite only a single slide 1 is depicted in Figure 5, it is likely that multiple slides 1 took place progressive, which may have resulted in the loss of the whole cross-section of the top fill somewhere along the crest length, which may have facilitated the start of over-topping flow. It is possible that, if slide 1 had not taken place, the over-topping flow would not have taken place as a result of the occurrence of slide 2. It is certain that this over-topping flow eroded very fast the top fill, which resulted in the breaching of the dam. The evidence for that slide 1 took place before slide 2 took place in the top and middle fills, as illustrated in Figure 5b, is that, as seen from Figure 6, it was found by an investigation performed after the earthquake, a number of large stones constituting a masonry riprap covering the upstream slope face of the top fill (Figure 1b) were covering the concrete panels, which were remained near the original place on the upstream slope face of the middle fill.

Figure 4c shows the structure of the old main dam inferred based on the results of invesitigations performed after the collapse. The old main dam has no core zone. Large part of the middle and bottom fills survived the over-topping flow. In comparison, the most of the backfill of the top fill was lost. However, small zones next to both banks of the top fill survived. The typical grading curves and the results of laboratory compaction tests that used the materials retrievd from these zones, together with the results of soil dry density measurments in the field, are presented in Figures 7a and b. The compaction enery level was Standard Proctor (1Ec) in the most compaction tests, while Modified Proctor (4.5Ec) was used only with the top fill material. The backfill material of the top fill, which was constructed after World War II (WWII), was sandy soil including only a small fines content (Fig. 7a). This fact is consistent with the observatoion that the top fill was eroded very fast by the overtopping flow (Figs. 4a & 5b). The degree of compaction was very low in the top fill: i.e. $(D_c)_{4.5Ec}$= 84 % and $(D_c)_{1Ec}$= 87.9 %. With a similar soil type of the top fill in the old auxiliarory dam, the $(D_c)_{1Ec}$ value was only 79.1 % (Fig. 8). These low $(D_c)_{1Ec}$ values are due probably to too low compaction energy. On the othear nad, an average $(D_c)_{1Ec}$ of the order of 95 % is usually achieved by modern earthwork performed to satisfy the allowable minimum value of 90 %, as specified in the old design code for agricultural irrigation dams (Ministry of Agriculture, Forestry and Fisheries, 2006). As shown later in this paper, in the resotration work of this dam that is following the new design code revised in 2015 (Ministry of Agriculture, Forestry and Fisheries, 2015), it is specified that all the measured values of $(D_c)_{1Ec}$ should be equal to at least 95 %.

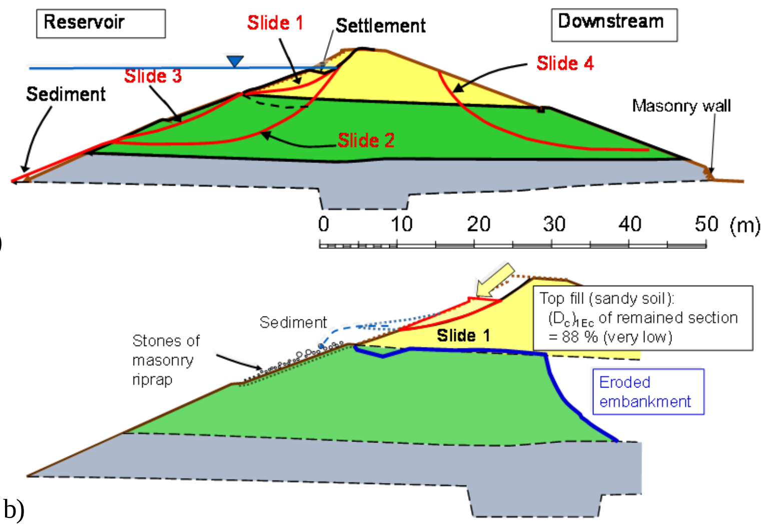

a)

b)

Figure 5. Inferred failure mechanism of old main Fujinuma Dam (Tanaka et al. 2012).

Figure 6. a) Views of upstream slope after collapse of old main Fujinuma Dam (taken by the first author).

The middle fill, which was completted before a break during WWII, consists of highly plastic silty soil. This soil types is appropriate to achieve a low hydraulic conductivity and a high resistance against erosion that are necessary as the backfill material for this type of earth-fill dam. This fact releaved by the post collapse investigation is consistent with the observation that the middle fill exhibited a relatively high resistance against erosion by the overtopping flow (Figs. 4a & 5b). However, the measured values of $(D_c)_{1Ec}$ of the middle fill are very low, not acceptable according to the old and new design codes. Theses low $(D_c)_{1Ec}$ values are due probably to that: a) the used compaction energy level was too low; and b) the water content during compaction was too high. The bottom fill is a fine sand including gravel, which was compacted best among the three fills of the old main dam, despite the earliest construction. Yet, the compaction is not satisfactory when based on the modern standard of earthwork.

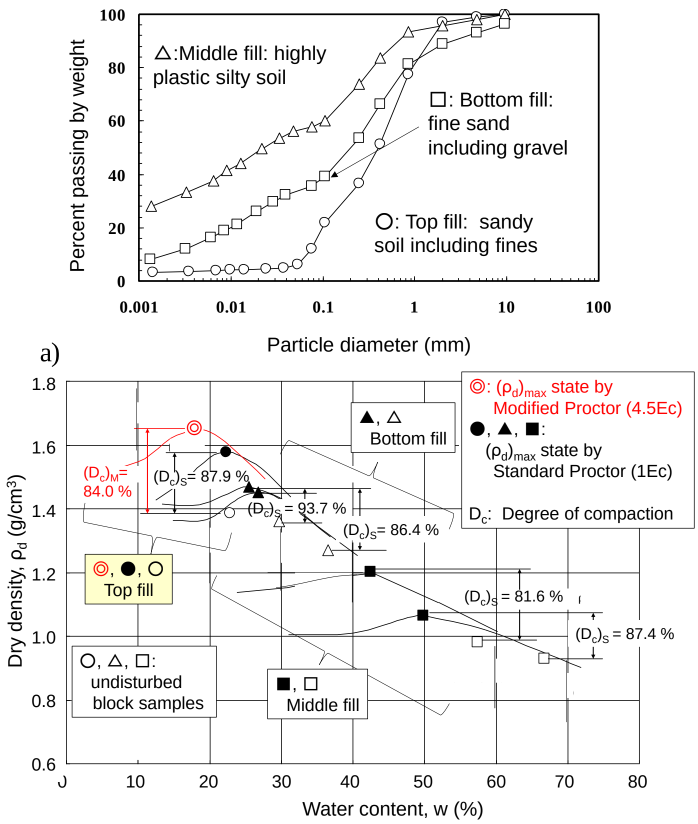

b)

Figure 7. a) Grading curves of top, middle and bottom fills of old main dam; and b) compacted states of three fills near the right bank, old main Fujinuma dam (Tanaka et al. 2012).

Based on the above, the causes for the collapse of the old main dam were inferred as follows:

1) The compaction was generally poor with all of the top, middle and bottom fills. This is due likely to no modern compaction control with too low compaction energy achievable at the time of compaction.
2) The soil type of the top fill is sandy soil, which is not the appropriate soil type, as it is highly liquefiable when loose and saturated; highly permeable; and highly erodible.

At the time of the earthquake, the water level in the reservoir was high prepared for the start of irrigating rice fields (Fig. 5a). So, the lower part of the top fill was saturated.

3) The likely scenario of collapse is as follows:
   a) In the saturated zone in the top fill, the undrained shear strength dropped significantly from an initial value, which is not high, by cyclic undrained loading during the earthquake.

b) Failure started in the top fill (slide 1 in Fig. 5). Probably multiple slides 1 took place progressively.
c) Immediately after event b), larger failure by slide 2 took place in the top and middle fills.
d) Events b) and c) resulted in the start of over-topping somewhere along the crest.
e) The scale of over-topping flow became larger quickly by fast erosion of the top fill.
f) The breaching of the whole dam took place causing a flood by the whole water impounded in the reservoir.

A slide occurred also in the old auxiliary dam, consisting of similar backfill materials as the old main dam (Fig. 8). Unlike the old main dam, over-topping flow did not take place. It is not certain whether this fact means that the slide in the old auxiliary dam took as a result of fast drawdown in the reservoir as a results of the beaching of the old main dam. It is also possible that the slide took place by seismic loads as the old main dam when the reservoir was fully impounded. This is because the slide was of such a flow type as the one that takes place under water (Tanaka et al. 2012).

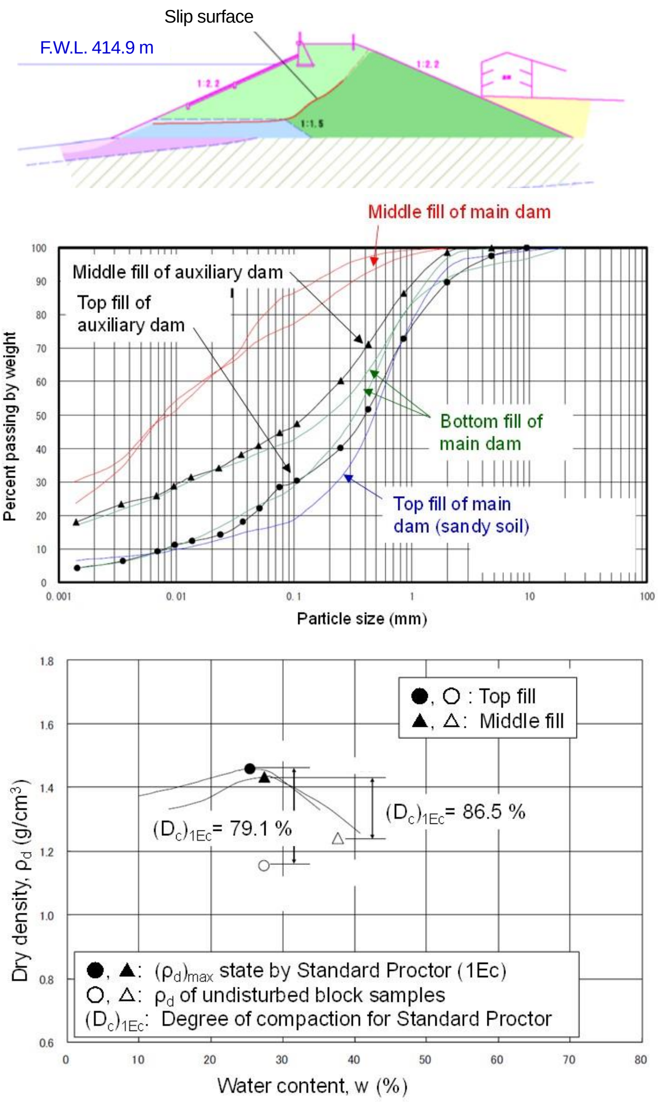

a) b) c)

Figure 8. a) Structure; and b) grading curves; and c) compacted states of two fill types (at the central part), the old auxiliray dam (Tanaka et al., 2012).

2.2 *Restoration of Fujinuma Dams*

2.2.1 *Design and construction to satisfy required seismic performance*

When evaluating the seismic stability of soil structures, including earth-fill dams, that are to be newly constructed or those currently existing in engineering practice, we often face problems resulting from an inconsistency between:

1) actual behavior reflecting actual soil stress-strain properties during an actual severe earthquake (or earthquakes); and
2) apparent behaviour evaluated by the conventional seismic design method using assumed soil stress-strain properties for specified (or assumed) seismic load.

In Figure 9a, these two behaviours are represented by two sets of points on the plane of soil shear strength, τ_f, and working shear stresses, τ_w. The safety factor, F_s. is defined by the ratio τ_f/τ_w. If the point is located below the line of F_s= 1.0, the concerned soil structure collapses by given seismic load. If the point is located above the line of F_s= 1.0, the concerned soil structure does not collapse. In this figure, letter A stands for a soil structure having well-compacted high-quality backfill with a high soil shear strength. It is assumed that soil structure A survives the actual severe seismic load defined as Level 2 seismic load (explained below). On the other hand, letter B stands for a soil structure having poorly-compacted low-quality backfill with a low soil shear strength. It is assumed that soil structure B collapses by the actual Level 2 seismic load. In Figure 9a, two values of τ_w caused by the following two different levels of design seismic load according to Japanese Society for Civil Engineers (1996) are indicated:

1) *Level 1 design seismic motion*: It is a seismic motion with a high likelihood of occurring during the design lifetime of the concerned structure. It is required that, in principle, all new structures have sufficient seismic resistance to ensure "no damage" when subjected to this seismic motion.
2) *Level 2 design seismic motion*: It is the strongest seismic motion thought likely to occur at the location of the concerned structure in the future. It is required that the structure should not collapse, although damage that renders it unusable is acceptable if its functionality can be rapidly restored.

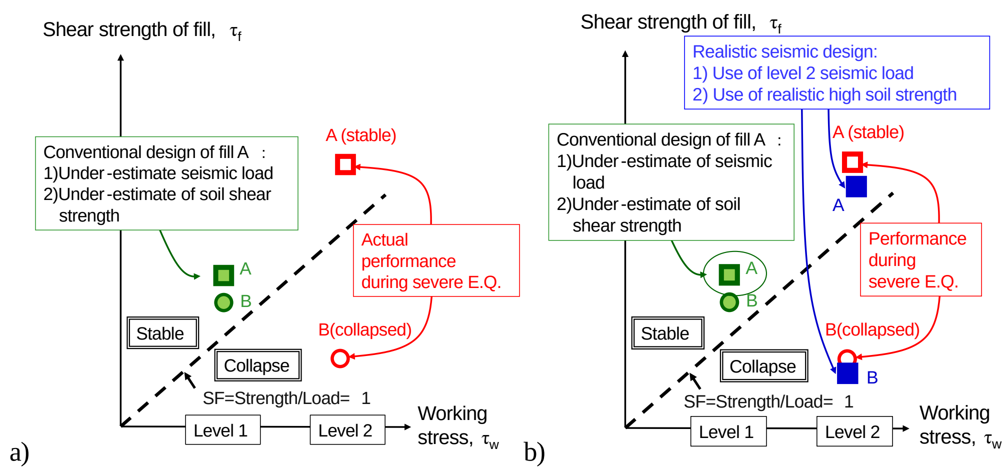

Figure 9. Schematic diagrams commparing: a) actural performance of well- and poorly constructed soil structuers and their conventional seismic designs; and b) actual performance of well- and poorly constructed soil structuers, their conventional designs and their newly proposed seismic designs.

Since the experience of serious geo-hazards in the 1995 Great Hanshin-Awaji Earthquake and later seismic events, there has been a gradual introduction of seismic design that take into account Level 2 design seismic motion for soil structures, foundation ground and the foundations of superstructures, although the timing of the change and the level of seismic resistance required are different with the type of soil structure and the organization responsible for it. With agricultural irrigation dams, the old code (Ministry of Agriculture, Forestry and Fisheries, 2006) specified that the stability is evaluated by the pseudo-static limit equilibrium-based stability analysis on the following conditions:

1) the design value of horizontal seismic coefficient, k_h, is equal to 0.15, which is today considered as Level 1 design seismic load;
2) the design soil shear strength, $(\tau_f)_d$, is the drained shear strength when $(D_c)_{1Ec}$ is equal to the allowable minimum value (e.g., 90 %) in compaction control; and
3) the required minimum factor of safety, F_s, is equal to 1.2.

The design code for agriculture irrigation dams was revised in 2015 (Ministry of Agriculture, Forestry and Fisheries, 2015). With important irrigation dams of which collapse may result in a serious disaster, the new code requires the use of: 1) a relevant Level 2 design seismic motion; and 2) undrained shear strength that may degrade by cyclic undrained loading with saturated soil. Then, the use of k_h= 0.15 is too low as Level 2 design seismic load.

With well-compacted soil structure A, the use of the shear strength that is under-estimated, for example, by the under-estimation of the $(D_c)_{1Ec}$ value, as the design value is on the safe side. So, the effects of an underestimation of seismic load and an under-estimation of soil shear strength on the calculated value of F_s may be balanced, resulting in a relevant F_s value as illustrated in Figure. 9a. In this case, if only the design seismic load is levelled up under otherwise the same conditions, this balance is lost and the F_s value is under-estimated. On the other hand, with poorly-compacted soil structure B (such as old Fujinuma dams), the effects of the following two factors are not balanced:

1) The use of k_h= 0.15 as Level 2 design seismic load is on the unsafe side.
2) The use of the shear strength when the dry density is higher than the actual value as the design shear strength. Besides, if saturated soil is sheared undrained during an earthquake, the use of drained shear strength as the design undrained shear strength is on the unsafe side.

Due to these factors on the unsafe side, a largely unsafe result (i.e. a largely over-estimated F_s value) is obtained. In this case, to obtain realistic results by the stability analysis, it is not sufficient to level up the design seismic load to Level 2, but it is also necessary to use realistic soil shear strength. With poorly-compacted soil, the realistic undrained shear strength is usually much lower than the corresponding drained shear strength.

Commonly with soil structures A and B, the relevant while realistic design should be based on the following procedures (Figure 9b):

a) Level 2 design seismic load relevant to a given soil structure is used.
b) Realistic soil shear strength, τ_f, corresponding to the actual average value of D_c, which is noticeably higher than the allowable lower bound (e.g. 95 %), is used. With saturated soil, τ_f could be either undrained or drained strength depending on the drainage condition in the field.
c) The stability is evaluated by comparing the calculated residual displacement/deformation of a given soil structure with the allowable limit specified in design.

When based on this method, the stabilities of soil structures A and B become largely different, unlike the conventional method following the old design code for agricultural irrigation dams. The results from the stability analysis following this methodology of the collapsed Fujinuma main dam are presented later in this paper. It has been required to restore the collapsed Fujinuma dams to those that are much more stable, being sufficiently stable against the severe seismic motion by which the old dams entirely collapsed. To satisfy this requirement, it becomes necessary to better compact backfill materials of higher quality and the relevant compaction control became imperative, as described in the next section. Obviously stability analysis based on the conventional method following the old design code is not able to show that the new dams have a much higher seismic stability the old dams while they are very stable against the severe seismic load by which the old dam fully collapsed. To design the new dams, the seismic stability was evaluated by the methods a), b) & c) described above, which can explain the collapse of the old main dam.

2.2.2 *Compaction control based on water content, dry density and degree of saturation*

The conventional fill compaction procedure usually controls the dry density, ρ_d, and the water content, w, relative to the maximum dry density, $(\rho_d)_{max}$, and the optimum water content, w_{opt}, determined by laboratory compaction tests performed at a certain compaction energy level (CEL) using a sample representative of concerned earthwork. However, $(\rho_d)_{max}$ increases and w_{opt} decreases with an increase in CEL. Since Proctor (1933), the maximum CEL practically available in the field has been increasing and the required ρ_d value has generally been becoming higher for more satisfactory performance of soil structures. Besides, the soil type may change in the field even when a fixed soil type is specified while the values of $(\rho_d)_{max}$ and w_{opt} change with inevitable changes in the soil type. So, even in a single earthwork project, the actual CEL and soil type may vary and it is very difficult to accurately estimate the field CEL and identify the actual soil type at a given moment at a given place. Therefore, the actual values of $(\rho_d)_{max}$ and w_{opt} at a given moment at a given place are usually unknown.

On the other hand, the following facts have been revealed by analysis of the results from a comprehensive series of laboratory and field compaction tests, CBR tests, laboratory stress-strain and permeability tests etc. of compacted soil (Tatsuoka 2015; Tatsuoka et al. 2016):

1) The optimum degree of saturation $(S_r)_{opt}$, defined as the degree of saturation, S_r, where the maximum dry density, $(\rho_d)_{max}$, is obtained for a given CEL and a given soil type, and the relationship between the true degree of compaction $(D_c)_t = \rho_d/(\rho_d)_{max}$ (x 100 %) and S_r - $(S_r)_{opt}$ obtained by compaction tests using a certain soil type at a certain CEL are essentially independent of CEL and insensitive to soil type variations.
2) The strength and stiffness before and after soaking, the hydraulic conductivity after saturation of compacted soil and the collapse deformation upon wetting are a function of the dry density, ρ_d, and "S_r at the end of compaction relative to the value of $(S_r)_{opt}$" (not a function of ρ_d and w) in addition to soil type in terms of particle size, grading etc.
3) Even at a given earthwork project where the soil type and the value of CEL are nominally fixed, the actual soil type and the actual CEL inevitably vary, thus the actual values of $(\rho_d)_{max}$ and w_{opt} at each location are variable and usually unknown. Despite the above, according to the facts 1) and 2), the value of $(D_c)_t$ and the physical properties of compacted soil at a given location can be estimated from measured values of ρ_d and S_r, without referring to the actual value of CEL and the actual soil type, if the value of $(S_r)_{opt}$ and the $(D_c)_t$ vs. S_r - $(S_r)_{opt}$ relation have been obtained by laboratory compaction tests on the representative sample using a certain CEL.

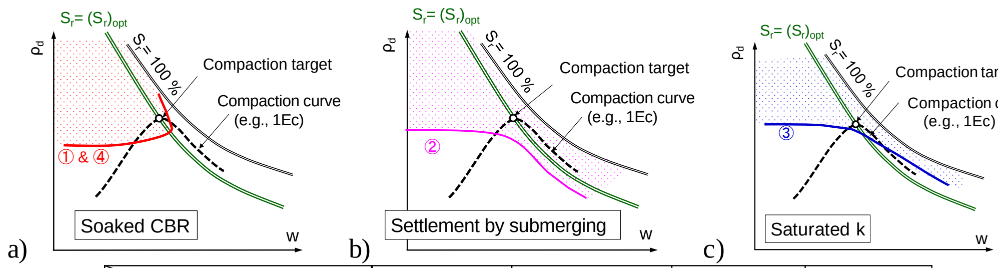

Control boundaries	Required properties of compacted soil	① High strength & stiffness	② Small collapse, & ②' small strength reduction upon wetting	③ Low permeability	④ No danger of over-compaction
For fill material to be compacted	WL for w	Important 1)	**Essential**	Important	
	WU for w	**Essential 2)**			**Essential**
For compacted fill	DL for D_c	**Essential**	Important	Important	Important
	SL for S_r		**Essential**	**Essential**	
	SU for S_r	Important			**Essential**

Notes 1) & 2): These control boundaries are either essential or important to achieve this soil property.

Figure 10: a) – c) Contours of allowable bounds of three typical soil properties often required in design and the corresponding acceptable or allowable zones (Tatsuoka 2015; Tatsuoka et al. 2016).

Based on the facts described above, Tatsuoka (2015) and Tatsuoka et al. (2016) proposed the following compaction control method for efficient compaction control, which is more efficient than the conventional method. Importantly, this method does not contradict the conventional soil compaction control, but it unifies several approaches in the conventional practice that are generally not well related to each other and/or apparently inconsistent with each other. The proposed method is characterized by the following features:

a) The compaction targets of S_r and ρ_d (or $(D_c)_{1Ec}$ for example) are determined by establishing a link between the soil compaction control and the design of soil structure (Fig.10). To this end, it is ensured whether the S_r value of compacted soil has become close to $(S_r)_{opt}$ while ρ_d becomes higher than the target value, $(\rho_d)_{target}$, by which the soil properties required in design are realized (Fig. 11a).

b) Not only ρ_d (or $(D_c)_{1Ec}$ for example) and S_r, but also w is controlled in a unified manner. The control boundaries of ρ_d, S_r and w are specified to deal with their inevitable scatters in actual earthwork projects (Fig. 10). They are related to each other in a consistent manner (Figure 11a).

c) The results from laboratory compaction tests performed at a specified CEL is the basis for the proposed compaction control. However, the proposed method is applicable to any other CEL values, while it is not required to evaluate the field CEL value, which is variable and very difficult to evaluate.

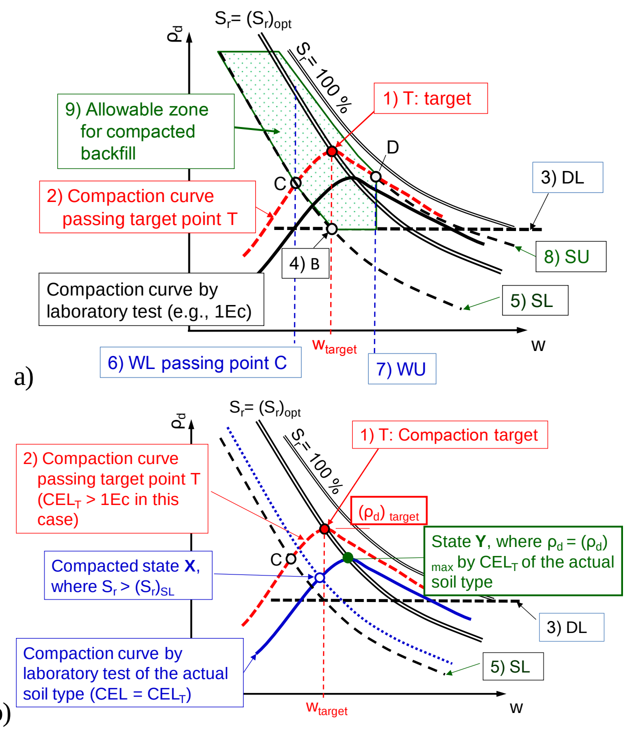

Figure 11: a) Soil compaction control to achieve the soil properties required in design of a given soil structure; and b) the true degree of compaction $(D_c)_t$ when CEL is well controlled to be constant equal to CEL_T (Tatsuoka 2015; Tatsuoka et al. 2016).

Figure 11a shows the overall picture of the soil compaction control procedure proposed based on the analysis shown above. This method comprises steps 1 – 9 depicted in this figure and explained below.

Step 1: Compaction target T is determined, where $S_r = (S_r)_{opt}$ (irrespective of CEL and soil type); and $\rho_d = (\rho_d)_{target}$, which can realize the required soil properties (Figure 10).

Step 2: The in-situ target compaction curve, which passes point T, is obtained by assuming that "the $\rho_d/(\rho_d)_{max}$ and S_r - $(S_r)_{opt}$ curve" is independent of CEL.

Step 3: The allowable lower bound for ρ_d, denoted as DL, is determined, where $D_c = \rho_d/(\rho_d)_{target}$ x 100 % is equal to a specified value, such as 95 %. Several sets of data as the rationales for 95 % is reported in Tatsuoka (2015). The purposes of setting DL and the others are listed in the table inset in Figure 10.

Step 4: Point B where w= "the value at target T, w_{target}" is obtained along DL.

Step 5: The constant S_r curve that passes point B is defined as the allowable lower bound for S_r, SL. SL crosses the target compaction curve at point C. Note that, if the allowable lower bound of S_r is specified to satisfy requirements for hydraulic conductivity, for example, and if this S_r

value is higher than the value at point B, the S_r value for SL (i.e., the S_r value at point C) is re-set to be equal to that S_r value.

Step 6: The allowable lower bound for w, WL, is specified to pass point C: i.e., w_{WL}= "w at point C".

Step 7: The allowable upper bound for w, WU, where $w= w_{WU}= w_{target} + x$, is specified to avoid too low strength/stiffness and to prevent over-compaction. Trial field compaction tests may be necessary to obtain the reliable value of x in each project. Only the fill material having w between w_{WL} and w_{WU} is allowed to be compacted.

Step 8: The allowable upper bound for S_r, SU, is specified to pass point D, where WU crosses the target compaction curve. Alternatively, the allowable upper bound for S_r, SU, is firstly specified as $(S_r)_{opt}$ + 5 %, for example, then point D is obtained where SU crosses the target compaction curve. Then, WU is obtained to pass point D.

Step 9: The acceptable or allowable zone for compacted soil comprising boundaries SL, DL, WU and SU is specified. Basically, WL is not necessary to define this zone. This is because compacted soils with $w< w_{WL}$ can satisfy the required soil proprieties if the compacted state is located in this allowable zone. In actuality, if $w < w_{WL}$, it is very difficult to reach this allowable zone even by compaction using a very high CEL. So, compaction using backfill having $w < w_{WL}$ is not allowed. On the other hand, if the compacted fill is required to be homogeneous to prevent differential deformation, the left part of the allowable zone may be truncated by WL, and/or an upper bound for ρ_d, DU, may be additionally specified.

Referring to Figure 11b, suppose that, in a given earthwork project, the value of CEL is always kept highly constant while close to the one for the target compaction curve (CEL_T). This condition is becoming more likely in recent well-controlled earthworks. Suppose that the current compacted state is found to be located at point X, where $S_r > (S_r)_{SL}$. The deviation of state X from the target compaction curve is due to that the actual soil type for point X is less compactable than the one for which the target compaction curve has been determined. The true degree of compaction, $(D_c)_t$, for CEL_T at state X is defined as "ρ_d at point X" / "ρ_d at point Y". "ρ_d at point Y" is equal to $(\rho_d)_{max}$ obtained by compaction tests using CEL_T of the actual soil type for point X. Then, even if state X is located much below the target point T, when state X is located close to DL, as far as $S_r > (S_r)_{SL}$, the $(D_c)_t$ value for CEL_T at state X is higher than the apparent D_c at state C (= "ρ_d at point C"/$(\rho_d)_{target}$), so this $(D_c)_t$ value at state X could be much higher than the allowable lower bound of D_c (typically 95 %). If the S_r value at state X is equal to $(S_r)_{opt}$, the $(D_c)_t$ value for CEL_T at state X is 100 %. This is one of the benefits obtained by maintaining the field CEL constant while controlling S_r to be close to $(S_r)_{opt}$.

It is believed that the proposed method is more practicable than the conventional method, so it makes the compaction control smoother. In particular, even if the water content is lower than w_{target}, compacted states become acceptable when $(D_c)_{1Ec}$ is equal to, or higher than, the specifiend allowable lower band while S_r is in between the allowable lower and upper bounds. So, this method encourages compaction to higher dry densities by using higher CELs at water contents lower than the optimum water content defined for CEL lower than field CEL. In the earthwork to restore the Fujinuma dams, the compaction control is being performed following this proposed method.

2.2.3 *Restoration work of Fujinuma dams*

The new Fukushima dams (Fig. 12) were designed to be much more stable than the old ones based on the stability analysis part of which is explained later in this paper. At the design stage, to determine the details of field compaction method, a series of field full-scale compaction tests were performed using the planned core material shown in Figure 13a. A compaction machine shown in Figure 13b was used. The following three different water contents were chosen to find the relevant water content for actual field compaction works: $w= (w_{opt})_{1Ec}$ (=18.5 %); $w= (w_{opt})_{1Ec}$ – 1.5 %= 17.0 %; and $w= (w_{opt})_{1Ec}$ + 4.0 %= 22.5 %. The field dry density and water content were measured in the soil layer immediately underlying the transient top soil layer (Fig. 13c). This metod was adopted to avoid errors by measuring these values in the transient top soil layer that includes the surface layer that has been highly remolded by the projections (called boots) on the drum while has not been well compacted by compaction work on the next soil layer. As seen from Figure 13d, over-compaction took place when compacted at w= 22.5 %, while the largest ρ_d value, slightly larger than $(\rho_d)_{max.1Ec}$, was obtained when w= 18.5 % and 17.0 %. Based on the above and to ensure sufficiently low hydraulic conductivity, the compaction target were determined in such that $(S_r)_{target}$= $(S_r)_{opt}$; w_{target}= $(w_{opt})_{1Ec}$ + 0.5 %; and $(\rho_d)_{target}$= "ρ_d when w= $(w_{opt})_{1Ec}$ + 0.5 %". This $(\rho_d)_{target}$ value is nearly the same as $(\rho_d)_{max.1Ec}$. In addition, the control boundaries (Fig. 10) were determined in such that: a) the allowable lower bound of $(D_c)_{1Ec}$ is equal to 95 %; b) the allowable lower and upper bounds of S_r are $(S_r)_{opt}$ – 5 % and $(S_r)_{opt}$ + 5 %; and c) the allowable lower and upper bounds of the water content, w, of the backfill to be compacted are $(w_{opt})_{1Ec}$ – 1.0 % and $(w_{opt})_{1Ec}$ + 2.0 %.

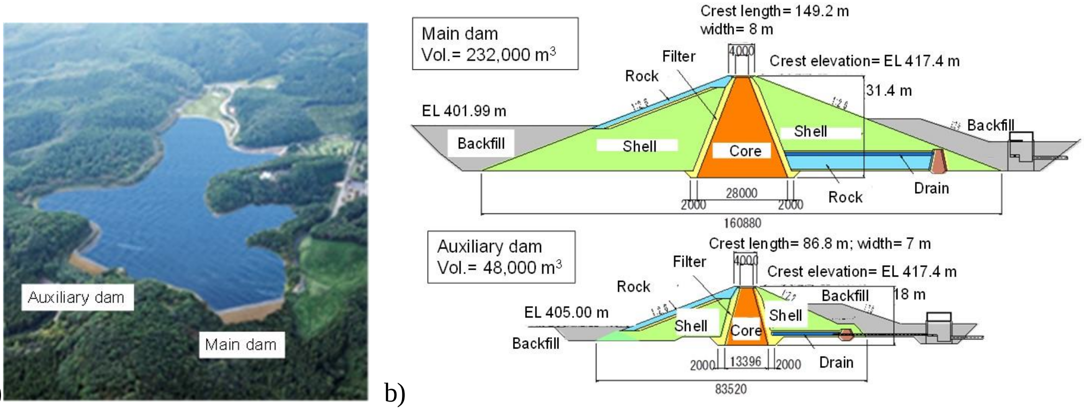

Figure 12: a) Artist' view; and b) typical cross-section of the restored main and auxiliary Fujinomori dams (Nagai et al. 2016; Santanbata et al. 2016).

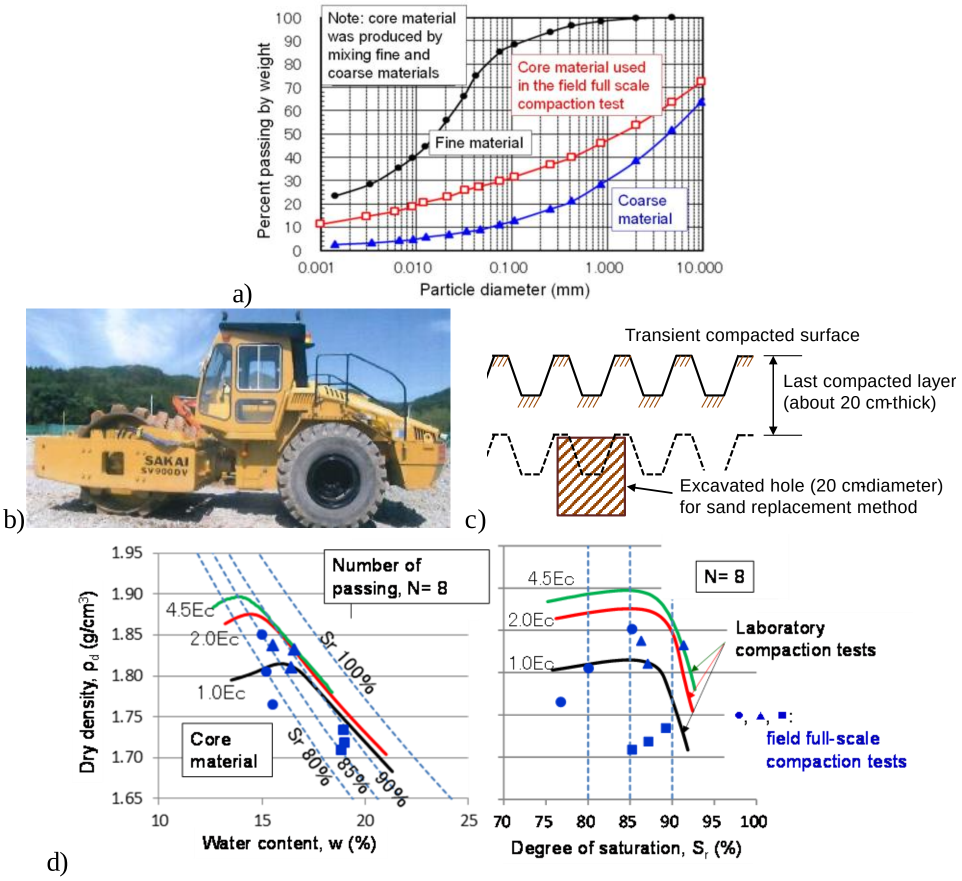

Figure 13: Feld full-scale compaction test of core material for Fujinuma dams: a) grading curve of core material; b) 20 ton-class vibratory tamping roller; c) measuring method of the field ρ_d and w values; and d) results of compaction at three different w values (Snatanbata et al. 2015; Nagai et al. 2015).

Figure 14a shows the grading curves of the core materials tested in the laboratory for field compaction control and those of the matrials actually used to construct the core zone of the new auxiliary dam. Figure 14b shows the distribution of compacted states in the actually constructed core zone together with the acceptable zone specified in advance. It may be seen that the compaction was performed satisfactorily. The field compaction energy level (CEL) was strictly controlled to be constant by monitorying by means of GPS installed to all the compaction machines. Therefore, a noticeably scatter seen in the data presented in Figure 14c is due mainly to a scatter in the grading chracteristics among the backfill materails as seen from Figure 14a. It is to be noted that, as explained above referring to Figure 11b, if the CEL is kept to a certain constant value, CEL_T, and S_r is maintained within the allowable upper and lower bounds, the scatter of the true degree of compaction, $(D_c)_t$ for CEL_T, is much smaller than the one of the values of apparent D_c seen in Figure 14b.

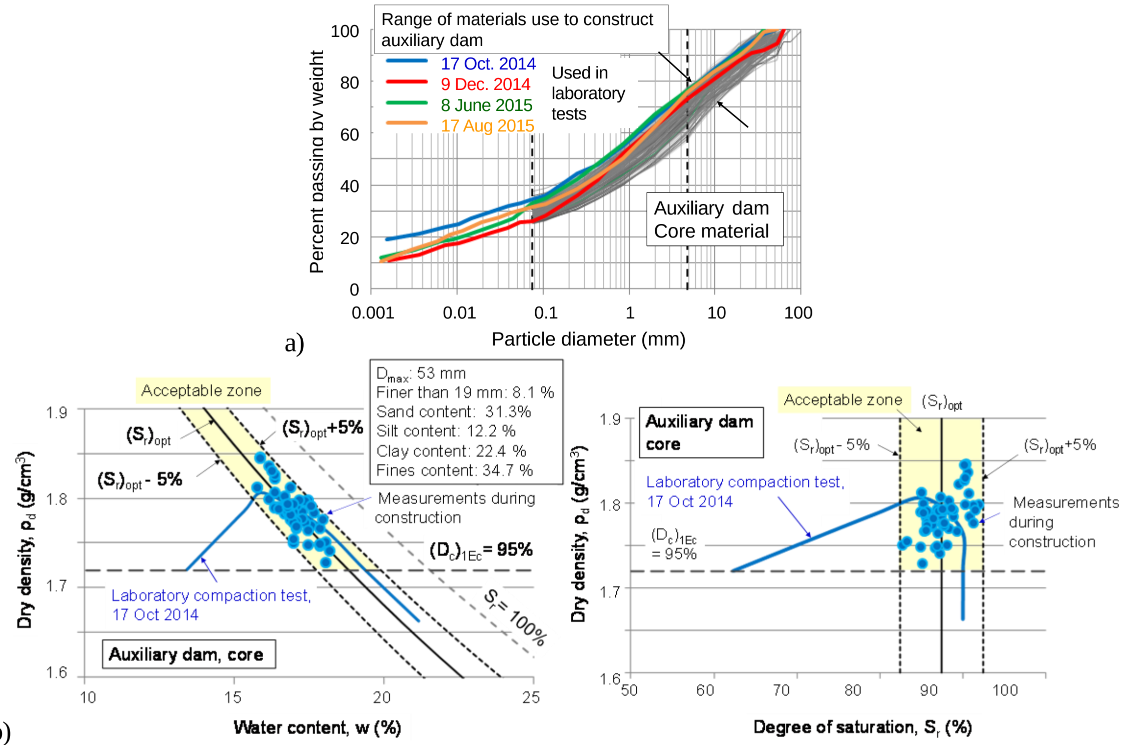

Figure 14: Compaction control in the construction of the core of Fujinuma auxiliary dam: a) grading curves of core materials tested in the laboratory and those used to construct the core; b) results of compaction after a number of passing equal to 8 (Snatanbata et al. 2015; Nagai et al. 2015).

Figure 15a shows the grading curves of the core materials tested in the laboratory and those of the matrials actually used to construct the shell zone of the new auxiliary dam. With the shell material, the compaction target was determined in such that $(S_r)_{target}= (S_r)_{opt}$; $w_{target}= (w_{opt})_{1Ec}$; and $(\rho_d)_{target}= (\rho_d)_{max.1Ec}$. The control boundaries (Fig. 10) were determined in such that: a) the allowable lower bound of $(D_c)_{1Ec}$ is equal to 95 %; b) the allowable lower and upper bounds of S_r are $(S_r)_{opt}$ – 15 % and $(S_r)_{opt}$ + 6; and c) the allowable lower and upper bounds of w for the back-fill to be compacted are $(w_{opt})_{1Ec}$ – 1.5 % and $(w_{opt})_{1Ec}$ + 1.0 %. The acceptable zone constituting of these boundaries is presented in Figures 15b and c. Figure 15b shows the distribution of compacted states in the actually constructed shell zone. Despite a very limited amount of data available at the time of writing this paper (August 2016), the data indicate that so far the soil compaction was performed satisfactorily.

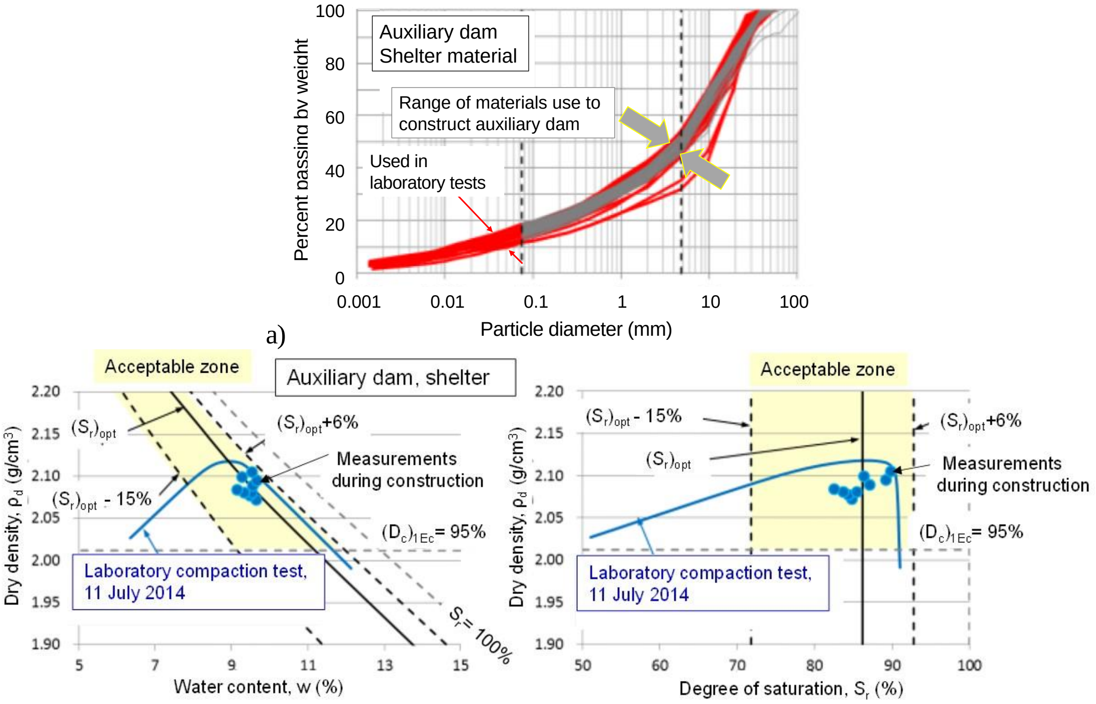

b)

Figure 15: Compaction control in the construction of the shelter of Fujinuma auxiliary dam: a) grading curves of core materials tested in the laboratory and those used to construct the shelter; b) results of compaction (Snatanbata et al. 2015; Nagai et al. 2015).

3 SOIL PROPERTIES OF OLD AND NEW FUJINUMA DAMS

3.1 *Old main dam*

3.1.1 *Stress – strain properties for stability analysis by Newmark-D method*

Following the method explained in Tatsuoka (2016), a series of monotonic and cyclic undrained triaxial tests were performed on specimens produced using samples retrieved from the top, middle and bottom fills of the old main dam (Ueno et al. 2013, 2014).

Table 2. Physical properties and specimen conditions of three soil types of old Fujinuma main dam (Ueno et al. 2013 & 2014).

	F_c (%)	U_c	U_c'	Plasticity index	ρ_d (g/cm³) ($(D_c)_{1Ec}$)	σ'_{rc}, σ'_{ac} (kPa)
Top fill: sandy soil including fines	12.0	7.4	0.9	NP	1.39 (87.9%)	35, 70
Bottom fill: fine sand including gravel	35.5	156.1	1.2	NP	1.32 (95.2%)	72, 144
Middle fill: highly plastic silty soil	57.8	-	-	31.6	0.96 (84.5%)	54, 107

Fc: fines content; U_c: coefficient of uniformity=D_{60}/D_{10}; U_c'=$(D_{30})^2/(D_{10}\cdot D_{60})$
$(D_c)_{1Ec}$= "compacted dry density ρ_d"/"$(\rho_d)_{max}$ by Standard Proctor (1Ec)"
σ'_{rc} & σ'_{ac}: initial effective radial & axial stresses at anisotropic consolidation

As listed in Table 2, the specimens were produced by compaction to the inferred field dry densities at w= $(w_{\text{opt}})_{\text{1Ec}}$ and made saturated using a back pressure equal to 200 kPa. The specimens were anisotropically consolidated to the estimated average stress state in the respective fills. The cyclic undrained triaxial tests were performed using a uniform symmetric sinusoidal wave at a frequency of 0.1 Hz. Figures 16a and b show two sets of typical undrained stress-strain behaviours before and after cyclic undrained loading. Figures 17, 18 and 19 show the summaries of the observed deviator stress – axial strain relations and the effective stress paths of the top, middle and bottom fill materials in undrained triaxial compression performed before and after the application of different cyclic undrained loading histories. It may be seen from Figures 17a, 18a and 19a that the initial undrained shear strength of the top and middle fill materials are particularly low when compared with that of the bottom fill material even when taking into account different initial effective stress levels. This trend of behaviour is consistent with the fact that the major slip took place in the top and middle fills (Fig. 5a). It may be also seen from Figures 16 ~ 19 that the monotonic undrained shear strength decreases with an increase in the maximum axial strain (defined as the damage strain) that has taken place by respective preceding cyclic undrained loading histories. It may also be seen from Figures 17b, 18b and 19b that the top and middle fill materials compacted to the respective inferred field dry densities exhibit a strong trend of contractive behaviour in the initial monotonic undrained loading. This result indicates that these materials were at rather poorly compacted states in the old main dam. In comparison, the bottom fill material exhibits a trend of dilative behaviour, showing that this material was at a relatively densely compacted state in the old main dam.

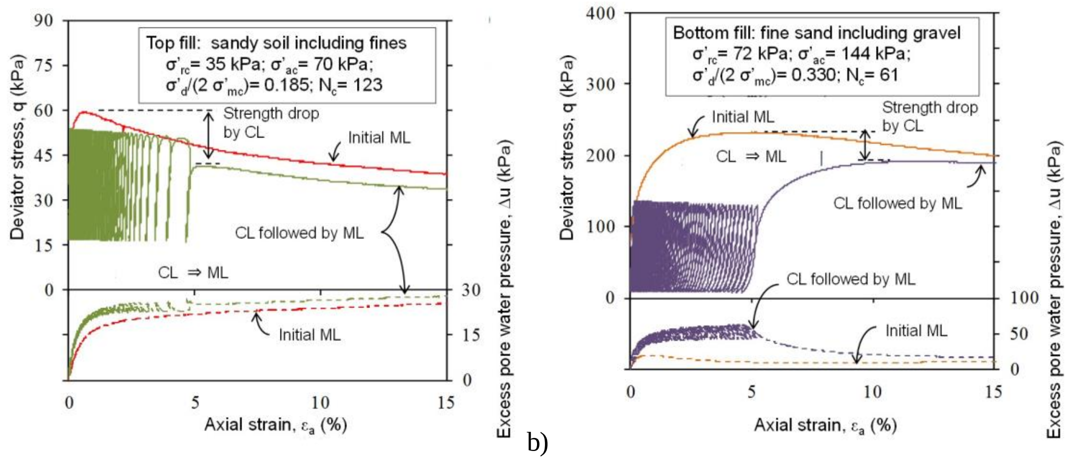

Figure 16. A typical set of undrained stress-strain behaviours before and after cyclic undrained loading: a) top fill; and b) bottom fill (Ueno et al. 2013 & 2014).

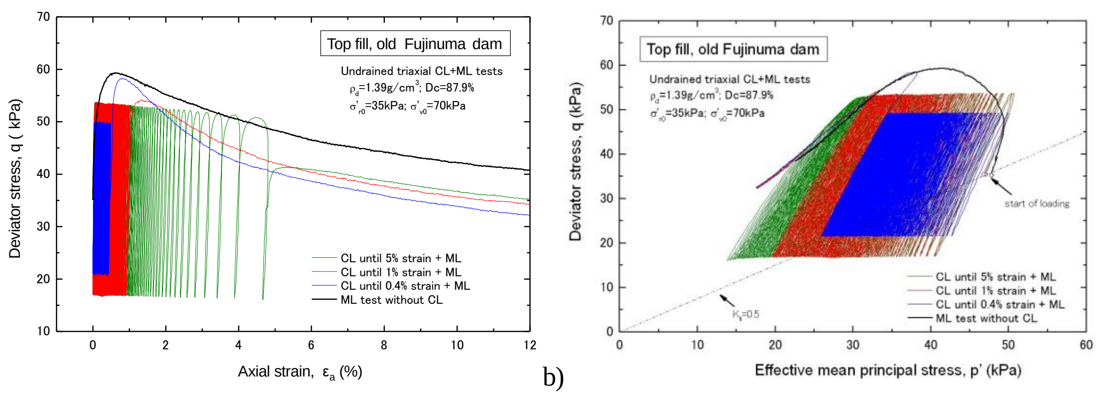

Figure 17. Sumamry of undrained stress-strain behaviours and effetive stress paths before and after applications of different cyclic undrained loading time histories, top fill material of old Fujinuma main dam (Ueno et al. 2013 & 2014).

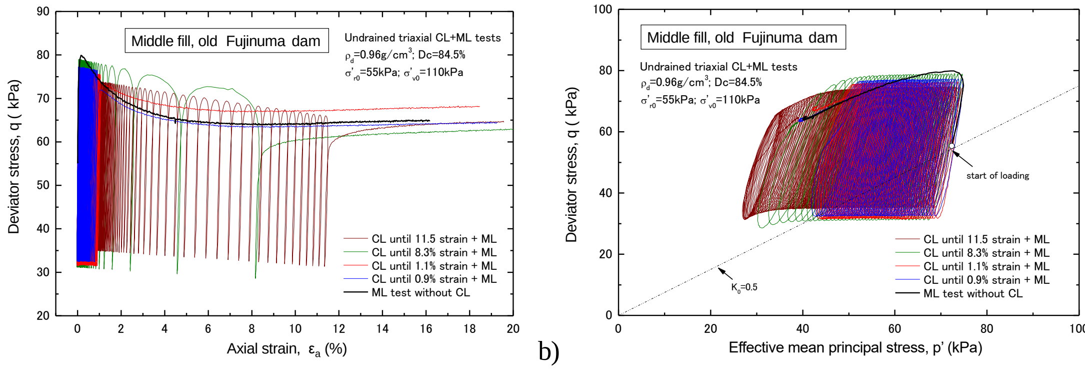

a) b)

Figure 18. Sumamry of undrained stress-strain behaviours and effetive stress paths before and after different cyclic undrained loading time histories, middle fill material of old Fujinuma main dam (Ueno et al. 2013 & 2014).

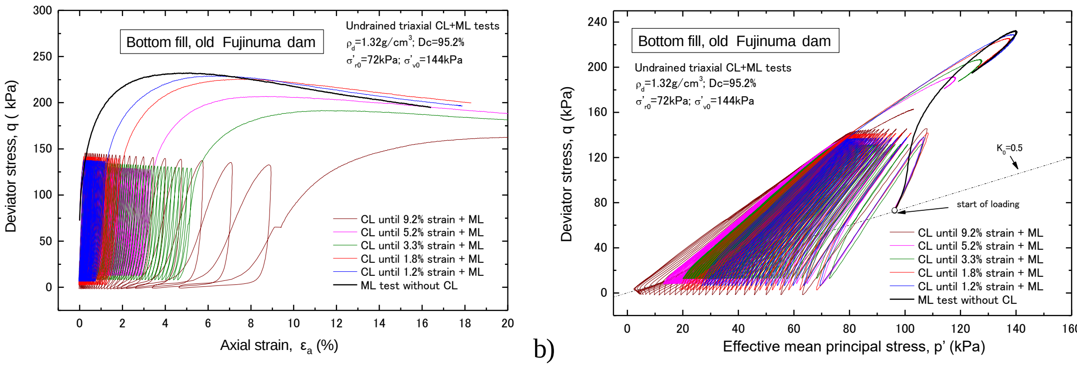

a) b)

Figure 19. Sumamry of undrained stress-strain behaviours and effetive stress paths before and after different cyclic undrained loading time histories, bottom fill material of old Fujinuma main dam (Ueno et al. 2013 & 2014).

Figure 20a shows the initial and damaged undrained shear strengths converted to an initial effective confining pressure σ'_c equal to 70 kPa plotted against $(D_c)_{1Ec}$. The damage undrained shear strengths shown in this figure are the minimum values observed in each monotonic undrained loading test after different cyclic undrained loading conditions. To so doing, it is assumed that the undrained shear strength is proportional to σ'_c. It may be seen that not only the initial undrained shear strength but also the damaged undrained shear strength increase significantly with an increase in $(D_c)_{1Ec}$, in particular with the bottom fill material. Besides, Figure 20b shows the relationship between “the minimum ratio of the damaged undrained shear strength to the initial undrained shear strength” and $(D_c)_{1Ec}$. It may be seen that the decrease in the undrained shear strength by the same cyclic undrained loading becomes smaller with an increase in $(D_c)_{1Ec}$. These trends of behaviour support the design policy for the new Fujinuma dams that the backfill is compacted much better than the old dams. In addition, for the same $(D_c)_{1Ec}$, the decrease in the undrained shear strength by the same cyclic undrained loading is smaller with the middle fill material (having the largest fines content) than the top and bottom fill materials (having the least and the second least fines content) (see Fig. 7a). Figure 20 c shows the relationship between the minimum ratio of the damaged undrained shear strength to the initial undrained shear strength” and “the ratio of the residual undrained shear strength to the initial peak undrained shear strength”. It may be seen that these quantities are reasonably correlated to each other. This means that, with an increase in the fines content, “the damaged undrained shear strength by cyclic undrained loading” less decreases associated with a smaller decrease in the residual undrained shear strength relative to the initial peak undrained shear strength. This result indicates that, conversely, the backfill material having a smaller fines content should be well-compacted when used for earth-fill dams.

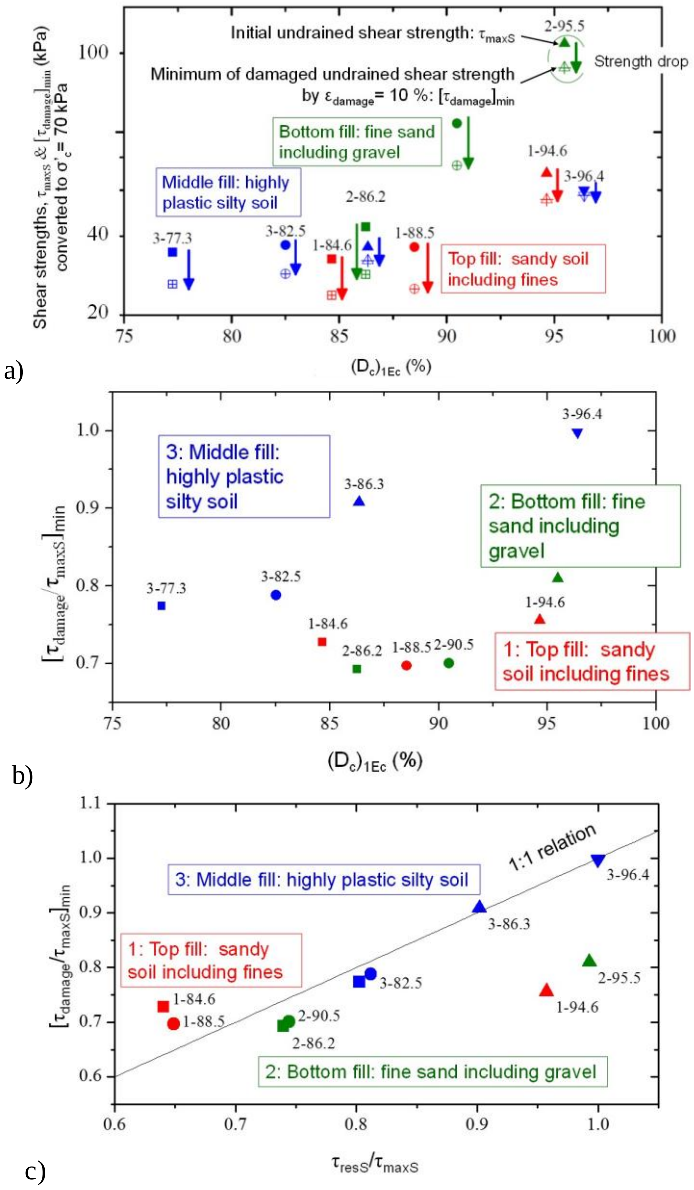

Figure 20. Relationships between: a) the initial and damaged undrained shear strengths converted to σ'$_c$= 70 kPa and $(D_c)_{1Ec}$; b) the minimum ratio of the damaged undrained shear strength to the initial undrained shear strength and $(D_c)_{1Ec}$; and c) the minimum ratio of the damaged undrained shear strength to the initial undrained shear strength and the ratio of the initial residual undrained shear strength to the initial peak undrained shear strength, the top, middle and bottom fill materials of old Fujinuma main dam (Ueno et al. 2013 & 2014).

Figure 21 shows the measured relationships between the ratio of the damaged undrained shear strength to the initial undrained shear strength and the damage strain and their fitted relations, which were used in the stability analysis of old Fujinuma main dam explained below. It may be seen that the deterioration rate decreases as the soil becomes more plastic or increases as the soil becomes less plastic. Figure 22 shows the relaionships between the SA cyclic stress amplitude and the number of loading cycles necessary to develop different maximum axial strains. It may be seen that the cyclic undrained strength is largest with the middle fill material, intermediate with the top fill material and smallest with the middle fill material, of which the order is opposite to that of the deterioration rate (Fig. 21). These results were used to obtain the time history of damage strain for the time history of random cyclic shear stresses obtained by the FEM response analysis based the cumulative damage concept in each FEM element in the dam.

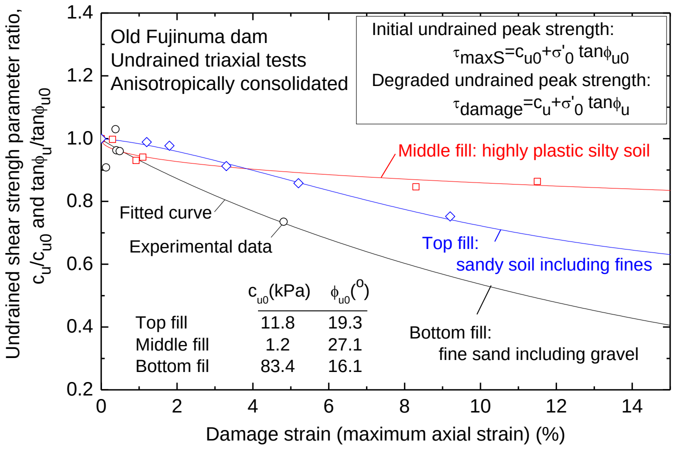

Figure 21. Measured and fitted relationships between the ratio of damaged undrained shear strength to initial undrained shear strength and the damage strain prepared for stability analysis of old Fujinuma main dam (Ueno et al. 2013 & 2014).

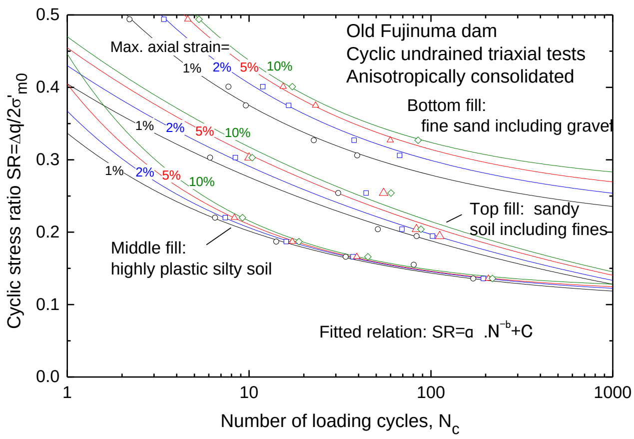

Figure 22. Measured and fitted relationships between the SA cyclic stress amplitude and the number of loading cycles to develop different maximum axial strains, anisotropically consolidated materials of old Fujinuma main dam (Ueno et al. 2013 & 2014).

3.1.2 *Stress – strain properties for stability analysis by pseudo-static non-linear FEM analysis*

Theoretical basis: Figure 23 shows results of a cyclic undrained torsional simple shear test on loose saturated Toyoura sand in which the specimen was K_0-consoldiated and cyclically sheared undrained at a constant shear strain rate equal to 0.1 %/min so that the physical quantities can be measured accurately. The time history of peak shear stress of a random wave of shear stresses that were proportional to the time history of acceleration recorded on the ground during the 1968 Tokachi-Oki earthquake was traced. So, the time histories of shear stress and other physical quantities recorded in the time domain (Figure 23b) were distorted from those that would have been obtained if cyclic stresses were applied by stress control to simulate the shape of the time history of seismic acceleration. In this cyclic undrained simple shear test, the shape and area of the cross-section and the height of the specimen were kept constant while only shear strain took place (Figure 23a). Figure 23c shows the effective stress path. Figure 23d shows the shear stress vs. shear strain relation. Figure 23e shows the relationship between the ratio of the shear stress to the effective vertical stress and the shear strain. Pradhan et al. (1988) reported similar results from a test on dense Toyoura sand.

It may be seen from Figure 23e that the whole behaviour exhibits smooth elasto-plastic strain-hardening stress-strain properties in which obvious yielding starts once the stress ratio, τ_{vh}/σ'_v, exceeds the previous maximum value in each shear direction (typically at points b and d), while the yielding in each shear direction is rather independent of the yielding in the other directoion. This trend of yielding can also be seen in the effective stress path (Fig. 23c) in that, before the start of dilatant behaviour, the σ'$_v$ starts decreasing upon the start of obvious yielding.

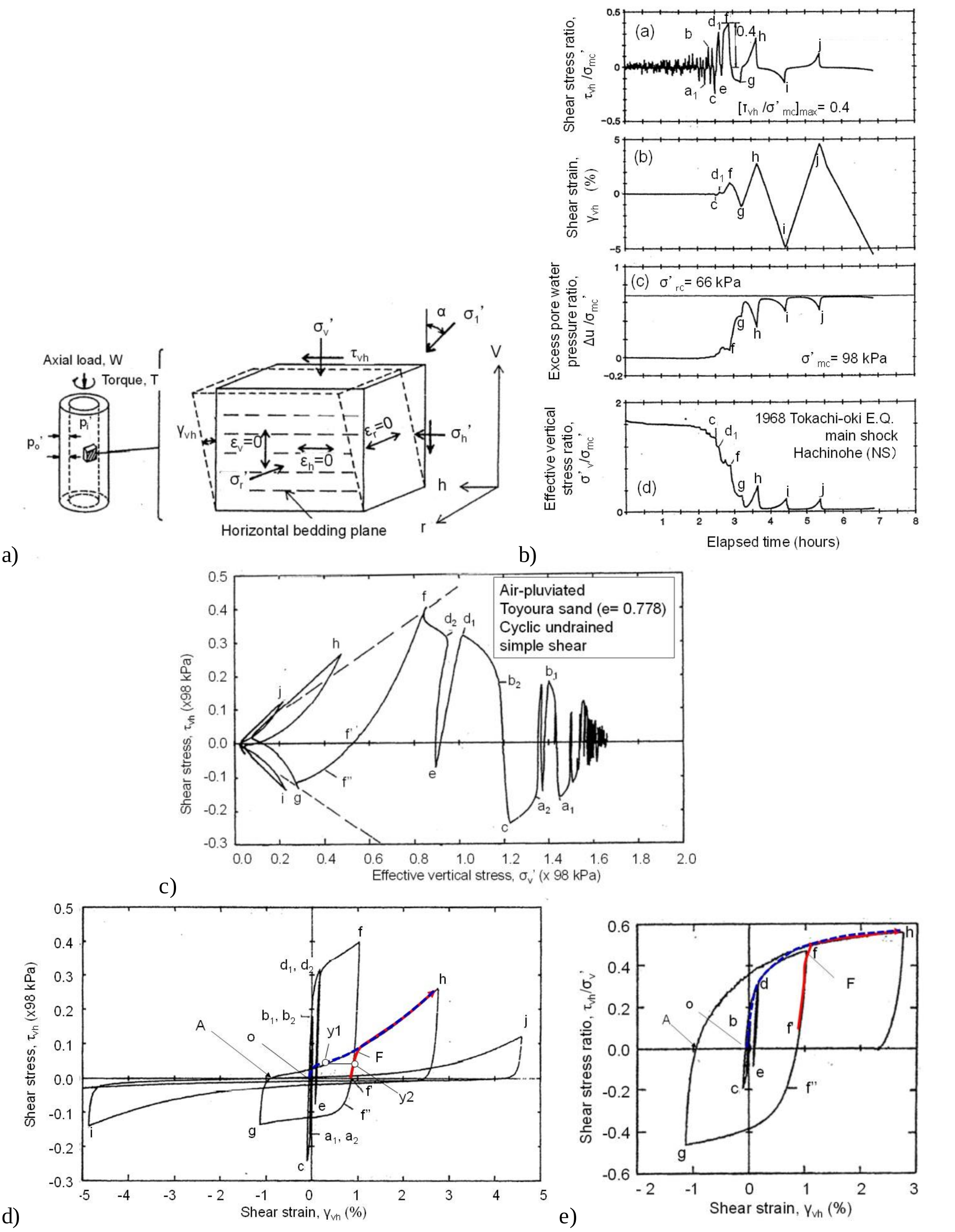

Figure 23. Cyclic undrained torsional simple shear test on loose Toyoura sand (constant shear strain rate= 0.1 %/min.): a) stress and strain conditions of hollow cylindrical specimen (20 cm in height; and 10 cm & 6 cm in outer and inner diameters); b) time histories of measured quantities; c) effective stress path; d) shear stress vs shear strain relation; and e) shear stress ratio vs. shear strain relation (Pradhan et al. 1988).

These results presented in Figure 23 indicate the following:

1) In Figure 23e, the τ_{vh}/σ'_v - γ_{vh} behaviour in the preceding cyclic loading process in which the shear strain is kept lower than, or equal to, the maximum shear strain, $(\gamma_{vh})_{max}$, that has taken place until the present time has essentially no effects on the τ_{vh}/σ'_v - γ_{vh} behaviour after the start of yielding (i.e. after γ_{vh} exceeds this $(\gamma_{vh})_{max}$ value). That is, the γ_{vh} value at point h that has taken place tracing a complicated τ_{vh}/σ'_v - γ_{vh} relation including many unload/reload branches starting from origin o toward point h is the same as the one that has taken place by monotonic loading tracing the reloading τ_{vh}/σ'_v - γ_{vh} relation f'→y2→F→h in a certain pulse during this cyclic loading.
2) As seen from Figure 23d, the γ_{vh} value at point y2 is much larger than the value at point y1 at the same τ_{vh}. This means that the τ_{vh} - γ_{vh} behaviour before yielding point F during reloading f'→y2→F→h is different from the behaviour before point F during monotonic loading starting origin (o→y1→F→h). However, as point h is reached after having passed point F, the same γ_{vh} value at point h as the one obtained by reloading f'→y2→F→h is obtained by monotonic loading starting from the origin (o→y1→F→h). This means that the $(\gamma_{vh})_{peak}$ value at each peak τ_{vh} states after yielding has restarted is obtained by monotonic loading that starts from the origin o that traces respective τ_{vh} - γ_{vh} relations that has deteriorated by preceding cyclic undrained loading, such as relation o→y1→F→h shown in Figure 23d.
3) In this way, the time history of $(\gamma_{vh})_{peak}$ observed at all the peak shear stress states in each shear direction, such as points b, d, f, h and j, is obtained.
4) As the τ_{vh}/σ'_v - γ_{vh} properties are elasto-plastic, the $(\gamma_{vh})_{peak}$ value observed at respective peak shear stress states is basically unrecoverable, becoming the residual shear strain, as far as the yielding does not takes in the opposite shear direction. This is particular the case in which the residual deformation tends to develop in one direction, such as the deformation of a slope.
5) The maximum value of $(\gamma_{vh})_{peak}$ may not be obtained when the applied peak shear stress is the maximum, but it may be obtained at a smaller peak shear stress after the stress – strain properties have deteriorated, as seen by comparing the $(\gamma_{vh})_{peak}$ values of at points f, h and j in Figure 23d.

The currently most sophisticated numerical analysis method to accurately simulate the response of a soil mass having undrained saturated zones is the effective stress analysis in the time domain by non-linear FEM. In this method, the whole effective stress path and the whole stress – strain relations, such as those presented in Figures 23c and d, in all FEM elements are fully traced while satisfying the stress/load equilibrium and strain/displacement-compatibility under given boundary conditions against the entire time history of given seismic load. This analysis is beyond the scope of this report.

On the other hand, the test results shown in Figure 23 suggest that an approximated value of ultimate residual deformation of a soil mass in which the residual deformation accumulates in one direction when subjected to a given seismic loading is obtained by the following simplified numerical analysis method. That is, the maximum deformations at peak seismic load states of such a soil mass as above are obtained by a series of pseudo-static non-linear FEM analyses of deformation due to monotonic loading by gravity forces and seismic loads. The respective stress – strain relations of soil in each element used in this analysis start from the origin (such as o→y1→F→h in Fig. 23d) while they continuously deteriorate during undrained cyclic loading. Then, the maximum value among the deformations at peak seismic load states obtained as above is considered as the ultimate residual deformation that is observed at the end of a given seismic loading history. If the soil properties are purely elastic, the maximum deformation is observed when the seismic load is maximum. When the stress – strain properties largely deteriorate during seismic loading, the maximum residual deformation may be observed in a pulse after the peak pulse has been passed (such as point j in Fig. 23d). In an extreme case, the maximum residual deformation takes place only by gravitational forces at the end of seismic loading.

Data of old main dam: Figure 24a, c and e show a set of normalized undrained shear stress vs. shear strain relations after different damage strains have taken place by respective preceding cyclic undrained loading histories of the top, middle and bottom fill materials of the old Fujinuma main dam. These monotonic stress – strain curves, which start from the origin such as o→y1→F→h depicted in Figure 23d, were obtained from the stress-strain relations observed in a series of cyclic-monotonic undrained triaxial tests depicted in Figures 17a, 18a and 19a In so doing, an initial relation starting from the origin was produced and made smoothly rejoined to the observed reloading behaviour, such as A→y1→F→h (Fig. 13d).

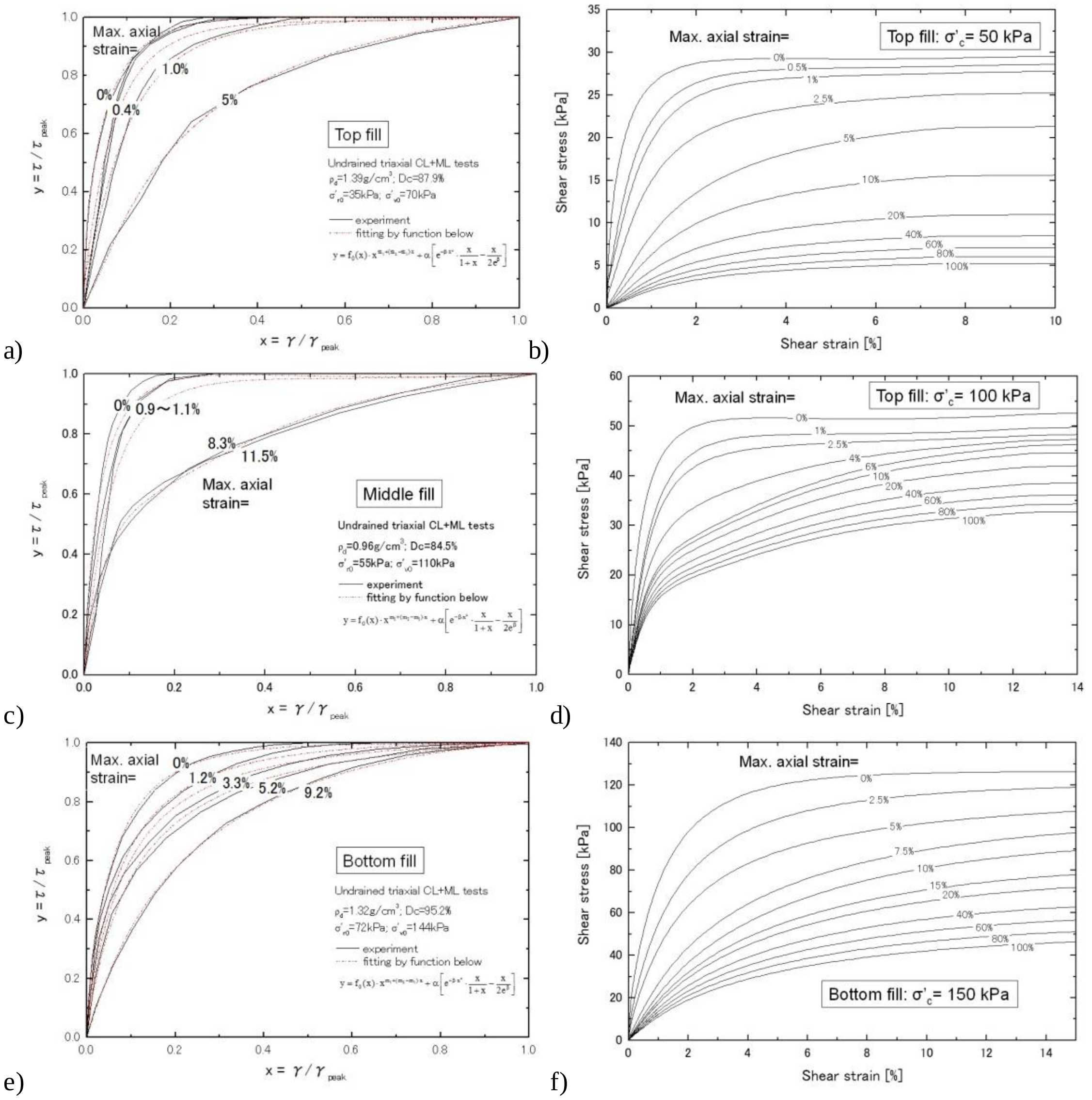

Figure 24: Normalized and non-normalized undrained shear stress vs. shear strain relations after different damage strains have taken place by cyclic undrained loading: a) & b) top fill; c) & d) middle fill; and e) & f) bottom fill of old Fujinuma main dam.

Figure 24b, d and f show a set of undrained shear stress vs. shear strain relations when σ'_c= 50 kPa or 100 kPa or 159 kPa obtained from the normalized relations shown in Figs. 24a, c and e. In so doing, when necessary, the damage strain was obtained by extrapolating to values larger than the largest value achieved in the experiments. To obtain the stress – strain relations starting from the same fixed origin where τ= 0 and γ= 0, the damaged undrained shear strength, τ_{max}, was first obtained based on the deterioration curves for the peak undrained shear strength presented in Figure 21. The measured peak shear strains, γ_{peak}, (as presented in Figs. 17a, 18a and 19a) were used except for the relations in which the damage strain exceeds the maximum value measured in the experiment. In that case, the value of γ_{peak} measured in the test that exhibited the largest damage strain was used. In addition, the post-peak strain softening was ignored in this modelling. This is because strain-softening takes place associated with slip displacements after the start of slip displacement along a failure plane (or failure planes) and they are analyzed by the Newmark method but not in the pseudo-stating FEM analysis. It may be seen from these figures that, for the same damage strain by cyclic undrained loading, the monotonic undrained stress – strain relation deteriorates more largely in the less plastic materials in the top and bottom fills than in the most plastic material in the middle fill. With the bottom fill, however, as the damage strain for the same cyclic stress ratio is smallest, the deterioration in the stress – strain relation is smallest. With the top fill, as the damage strain for the same cyclic stress ratio is intermediate, the deterioration in the stress – strain relation becomes largest when subjected to relatively large cyclic stresses.

3.1.3 *Other data*

Table 3 shows the summary of the properties of the materials in the zones 1 - 6 indicated in Figure 25. They were obtained by the series of laboratory stress-strain tests explained above and others. The values of c’ and φ’ were evaluated based on the effective stress paths obtained by a series of consolidated undrained triaxial compression (TC) tests, which are considered to pass immediately below the effective stress envelop (Ueno et al. 2013 & 2014). Part of these effective stress paths is presented in Figures 17b, 18b and 19b. These data were used in the stability analysis described later in this report. Note that the values of c’ and φ’ obtained by this way are usually slightly lower than the values obtained by drained TC tests under otherwise the same conditions with the difference increasing with an increase in the compacted dry density.

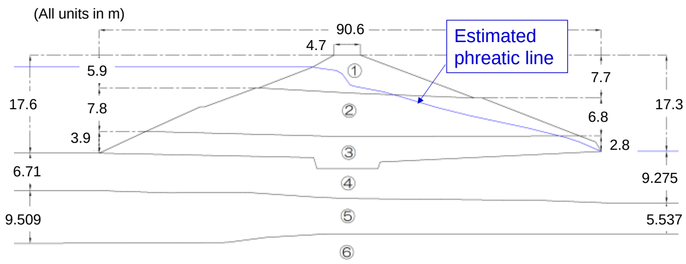

Figure 25. Analyzed cross-section of old Fujinuma main dam.

Table 3. Summary of the properties used in the stability analysis of old Fujinuma main dam (after the data obtained by Ueno et al. 2013 & 2014).

		γ_t (kN/m^3)	γ_{sat} (kN/m^3)	$[D_c]_{1Ec}$※ (%)	SPT-N	c' (kPa)	Φ' (deg)
①	Upper embankment	16.8	18.4	87.9	2	9.5	22.9
②	Middle embankment	13.9	15.7	84.5	5	0.6	27.9
③	Lower embankment	16.4	17.9	95.2	4	0.1	40.5
④	Non volcanic clay	21.7	20	-	13	31	32.5
⑤	Volcanic weathered gravel※2	17.7	17.7	-	19	44	37.3
⑥	Volcanic weathered granite※2	19.6	19.6	-	>50	-	-

※1 based on standard Proctor tests (1.0Ec), ※2 Quartenary early diluvium Shirakawa stratum

3.2 *New main dam*

3.2.1 *Stress – strain properties for stability analysis by Newmark-D method*

Figure 26 shows the cross-section of the new Fujinuma main dam for which the stability was analyzed. Figure 27 shows the grading curves of the core and shell materials. Table 4 summarizes the properties used in the stability analysis shown below. The soil properties reported herein are those obtained by laboratory tests using backfill materials planned to be used to construct the new dams at the design stage. Their soil types and stress-strain properties of the specimens compacted to their planned compacted states may be somehow different from those actually achieved in the construction. Analysis based on the soil types actually used to construct the new dams and their stress –strain properties when compacted to the actual states will be performed in due course in the near future.

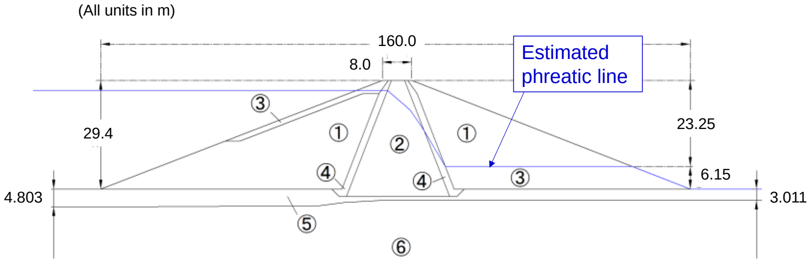

Figure 26. Analized cross-section of new Fujinuma main dam.

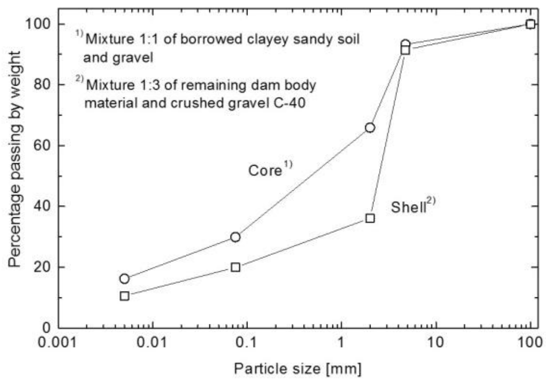

Figure 27. Grading curves of core and shell materials of new Fujinuma dams planned to be used at the design stage.

Table 4. Summary of the properties used in the stability analysis of new Fujinuma main dam.

		γ_t (kN/m³)	γ_{sat} (kN/m³)	D_c (%)	c' (kPa)	Φ' (deg)	c_u (kPa)	Φ_u (deg)
①	Shell	21.1	21.3	100※1	0	40.6	104.7	29.1
②	Core	20.3	20.8	100※2	5.6	36.0	108.7	45.5
③	Rock※3	20.5	23.0	-	9.3	41.4	9.3	41.4
④	Filter※4	19.9	22.3	-	48.8	43.1	48.8	43.1
⑤	Volcanic weathered gravel	17.7	17.7	-	44	37.3	44	37.3
⑥	Volcanic weathered granite	19.6	19.6	-	-	-	-	-

※1 compacted at w= w_{opt} + 2 % based on Standard Proctor tests (1.0Ec),
※2 compacted at w= w_{opt} based on twice Standard Proctor tests (2.0Ec),
※3,4 parameters based on typical rock and filter materials used in neighbouring dams

Figures 28 and 29 summarize the observed stress - strain relations of the core and shell materials compacted to, respectively, $(D_c)_{2Ec}$= 100 % and $(D_c)_{1Ec}$= 100 % (Table 4) and isotropically consolidated to an effective confining pressure equal to 130 kPa. It may be seen by comparing these figures with Figures 17a, 18a and 19a that their undrained shear strengths are substantially higher than those of the old main dam consolidated to similar effective pressure levels. Figure 30 shows the deterioration properties: i.e. the measured and fitted relationships between the ratio of the damaged undrained shear strength to the initial undrained shear strength and the damage strain. It may be seen by comparing Figures 21 and 30 that the specimens for the new dams, which are much better compacted, exhibit smaller reduction rates for the same damage strain by preceding cyclic undrained loading. This trend is consistent with the one reported in the companion paper (Tatsuoka 2016). Figure 31 shows the relationships between the SA cyclic stress amplitude and the number of loading cycles necessary to develop different maximum axial strains of the specimens of the new dams. Comparing Figures 22 and 31, it may be seen that the strength against cyclic undrained loading of the well-compacted specimens of the new dams are substantially higher than those of the poorly-compacted specimens of the old dam.

A noticeable drop in the undrained shear strength by preceding cyclic undrained loading may be seen in the data presented in Figures 28 and 29. Despite the above, it can be anticipated that, even when subjected to a strong seismic motion, high undrained shear strengths can be maintained due to: a) high initial undrained shear strengths; b) small damage strains by cyclic undrained loading; and c) small reduction rates of undrained shear strength by damage strain. Table 3 summarizes the properties obtained by this series of laboratory stress-strain tests that were used in the stability analysis.

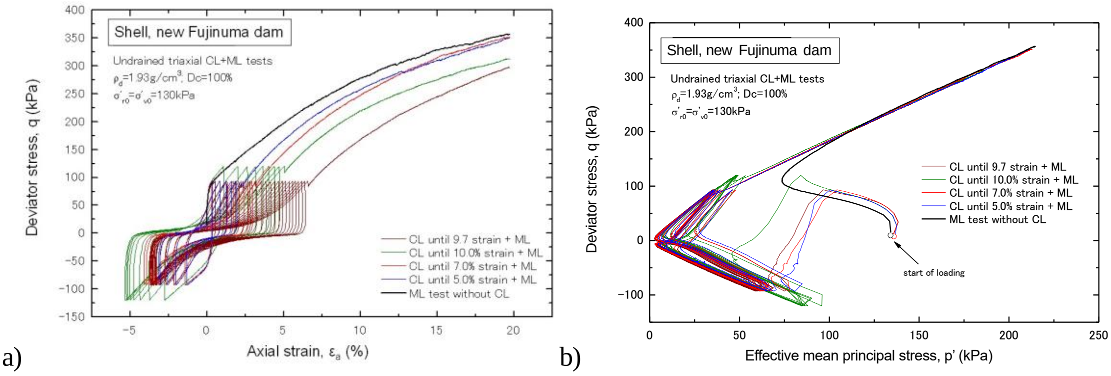

Figure 28. Sumamry of undrained stress-strain behaviours and effetive stress paths before and after applications of different cyclic undrained loading time histories, shelter material of new Fujinuma dams.

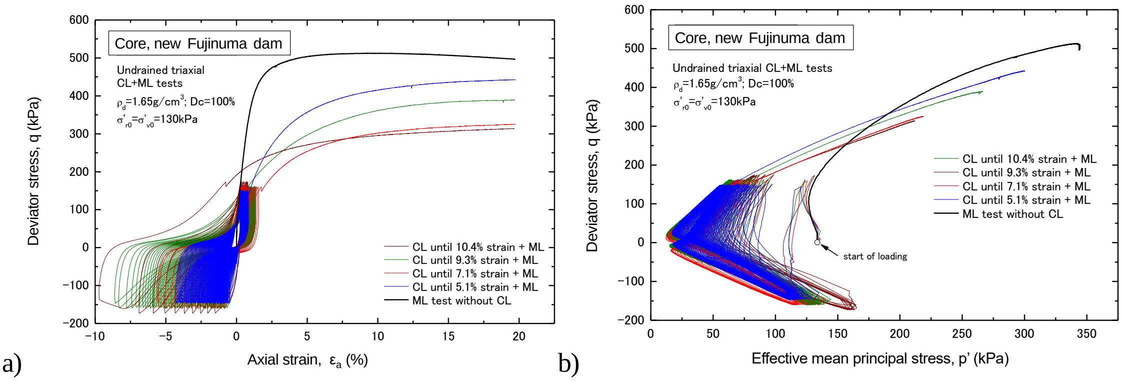

Figure 29. Sumamry of undrained stress-strain behaviours and effetive stress paths before and after applications of different cyclic undrained loading time histories, core material of new Fujinuma dams.

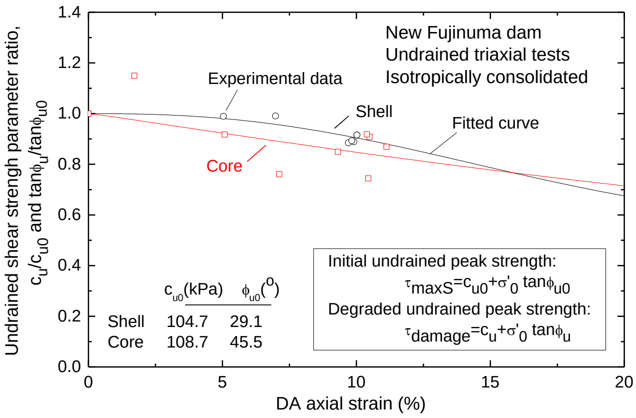

Figure 30. Measured and fitted relationships between the ratio of damaged undrained shear strength to initial undrained shear strength and the damage strain of isotropically consolidated specimens of core and shelter materials used in the stability analysis of new Fujinuma main dam.

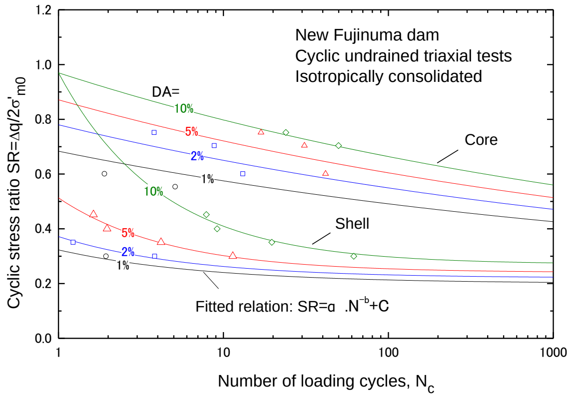

Figure 31. Measured and fitted relationships between the SA cyclic stress amplitude and the number of loading cycles to develop different maximum axial strains of isotropically consolidated specimens of core and shell materials used in the stability analysis of new Fujinuma main dam.

3.2.2 *Stress – strain properties for stability analysis by pseudo-static non-linear FEM analysis*

Figure 32 shows the normalized and non-normalized undrained shear stress vs. shear strain relations after different damage strains by cyclic undrained loading of the core and shell materials of the new Fujinuma dams, obtained from the results presented in Figures 28 and 29. Although the stress – strain relations deteriorate noticeably in these soil models, when compared with the similar relations for the old main dam (Figure 24), a large deterioration toward a very small strength does not take place in the analysis due to the following three mechanisms resulting from good compaction: a) high initial undrained shear strengths; b) small damage strains by cyclic undrained loading; and c) small reduction rates of undrained shear strength by damage strain.

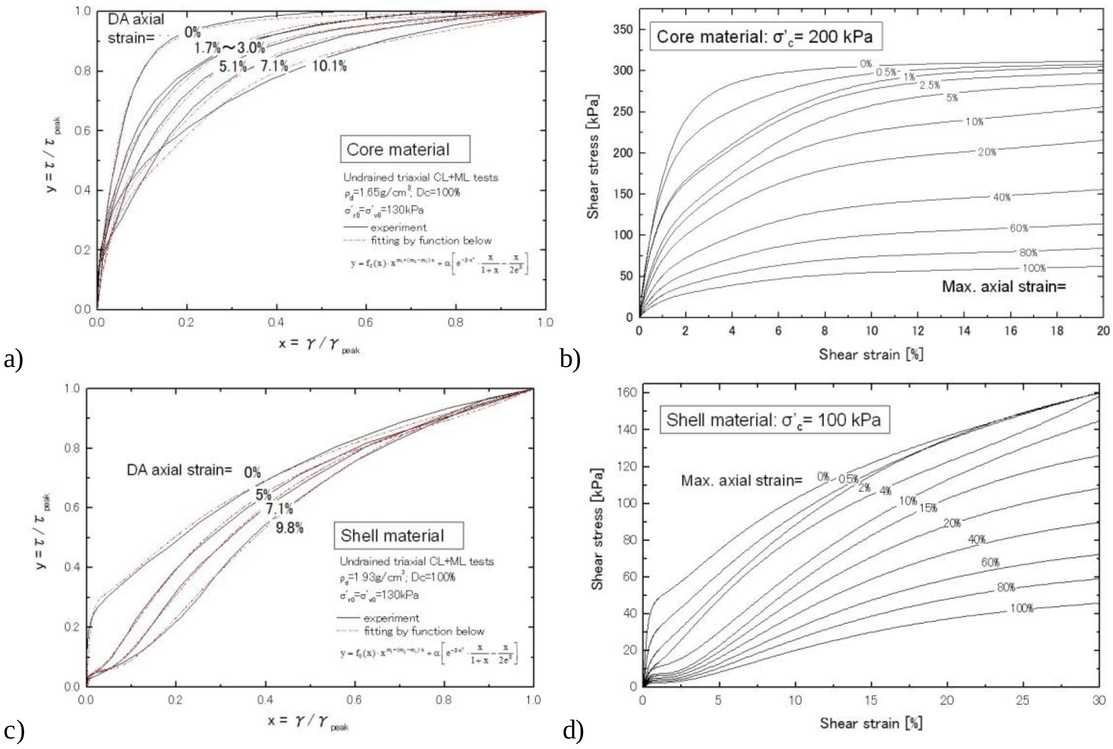

Figure 32. Normalized and non-normalized undrained shear stress vs. shear strain relations after different damage strain by cyclic undrained loading: a) & b) core material; and c) & d) shell material of new Fujinuma dams.

4 SLIP DISPLACEMENT ANALYSIS BY NEWMAK-D METHOD

4.1 *Old main dam*

4.1.1 *Safety factor for Level 1 design seismic load*

As an index of seismic stability, the global safety factor, F_s, for circular slip failure under drained condition was obtained by the so-called modified Fellenius method represented by:

$$F_s = \mathrm{Min.}\left[\frac{\sum[c'_{fi}\cdot l_i + (W'_i\cdot\cos\alpha_i - k_h\cdot W_i\cdot\sin\alpha_i)\cdot\tan\phi'_i]}{\sum(W_i\cdot\sin\alpha_i) + k_h\sum(W_i\cdot y_i/R) - M_w}\right] \tag{1}$$

where, for slice i, c'_{fi} and φ'_{fi} are the effective cohesion intercept and the angle of internal friction defined in terms of effective stresses; l_i is the length of slice base; W'_i is the effective weight, equal to the total weight, W_i, minus the buoyant force; α_i is the angle of slice base direction relative to the horizontal direction; k_h is the horizontal seismic coefficient; y_i is the arm length of k_h to the center of slip circle; R is the radius of slip circle and M_w is the moment about the center of slip circle by the total water pressure acting on the slope surface of the sliding mass. In this analysis, effects of seepage forces on the resisting moment are ignored. M_w is zero with the downstream slope, while it is large with the upstream slope. "Min." in Equation 1 means the minimum value with respect to the size and location of slip circle at respective peak stress states. It was confirmed that the results obtained by Equations 1 and 2 are essentially the same:

$$F_s = \mathrm{Min.}\left[\frac{\sum[c'_{fi}\cdot l_i + (W'_i\cdot\cos\alpha_i - k_h\cdot W_i\cdot\sin\alpha_i)\cdot\tan\phi'_i]}{\sum(W_i\cdot\sin\alpha_i) + k_h\sum(W_i\cdot y_i/R)}\right] \tag{2}$$

Herein, results obtained by using Equation 1 are presented. Figure 33 shows the stability of the old main dam against Level 1 design seismic load specified in the current code (i.e., k_h= 0.15) obtained by using drained shear strengths that are as representative as possible of those of the poorly compacted fills. The obtained drained F_s value is very low. Note that the drained condition is assmuned instead of the undrained condition, which is more likely with saturated soil in this case. Moreover, this value may have been affected by many uncertain factors, including the field dry density, as discussed in Tatsuoka (2016). The location of the critical slip circle obtained by the analysis is similar to the actual one named slip 2 in the upstream slope shown in Figure 5a. Residual slip displacement equal to 53 cm was evaluated by the Newmark-O method using constant drained shear strength against working shear stresses obtained by the earthquake response analysis using the inferred 'actual' seismic load (explained below). Although this residual slip displacement is not small, it cannot explain very large residual deformation of the main dam that took place during the earthquake.

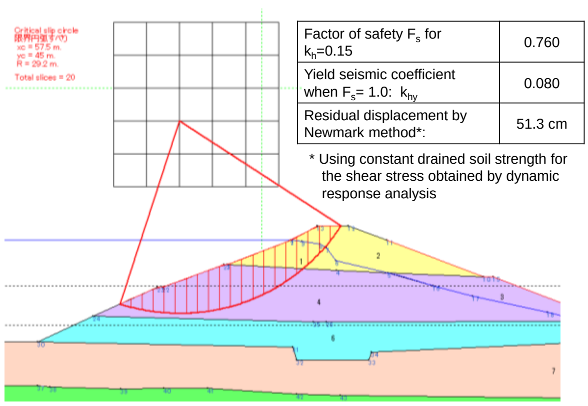

Figure 33. Drained stability against Level 1 design seismic load by Equation (1) of old Fujinuma main dam.

The drained F_s against k_h= 0.15 obtained by the stability analysis based on Equation 1 using the data presented in Table 4 is equal to 0.76. These soil properties data were obtained by a series of CU TC tests performed in 2012 and 2013 (Ueno et al. 2013 & 2014). On the other hand, Tanaka et al. (2014) reported that the drained F_s value against k_h= 0.15 of the collapsed main dam calculated by the limit equilibrium analysis is equal to 1.15. This F_s value was obtained by using another data set obtained by CU TC tests performed by another organization in 2011. The drained F_s against k_h= 0.15 obtained by the stability analysis based on Equation 1 while using the data used by Tanaka et al. (2014) is equal to 1.172. This difference is due to the use of different equations to obtain F_s values (this point is beyond the scope of this paper). The different between F_s= 0.76 and 1.172 is due to differences in the two sets of strength parameters. The reason for this difference is unknown. For a consistency, throughout this report, the results obtained by analyses using the data presented in Table 4 are reported.

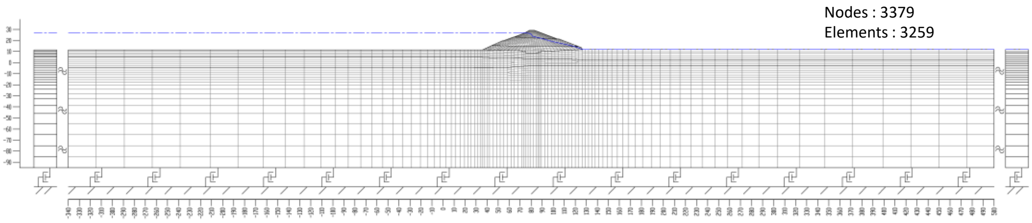

Figure 34. FEM model for static stress analysis, equivalent-linear seismic response analysis and pseudo-static residual deformation analysis of old Fujinuma main dam.

Table 5. Soil models for static stress analysis, equivalent-linear seismic response analysis of old Fujinuma main dam.

		γ_t (kN/m³)	γ_{sat} (kN/m³)	For static stress analysis		For dynamic response analysis		
				E (MPa) ※1	ν	G_0 (MPa) ※2	ν※2	G-h-γ properties
①	Upper embankment	16.8	18.4	5.6	0.3	50	0.353	Holocene epoch sand ※3
②	Middle embankment	13.9	15.7	14.0	0.45	37.9	0.364	Holocene epoch clay ※3
③	Lower embankment	16.4	17.9	11.2	0.3	67.2	0.491	Holocene epoch sand ※3
④	Non volcanic clay	21.7	20	7.0	0.45	49.6	0.469	Pleistocene epoch clay ※3
⑤	Volcanic weathered gravel※4	17.7	17.7	23.0	0.3	150	0.441	Pleistocene epoch gravel ※3
⑥	Volcanic weathered granite※4	19.6	19.6	143.0	0.3	380	0.449	Constant h=2.0%

※1 based on SPT-N values (E=2800·N, Japan Foundation Design Guidelines (2001) (Yoshinaka, 1968)
※2 based on field shear wave velocity measurements by PS logging
※3 empirical relations from Japan Public Work Research Institute (PWRI, Iwasaki et al. 1978 & others)
※4 Early Pleistocene epoch in Quaternary period, Shirakawa stratum

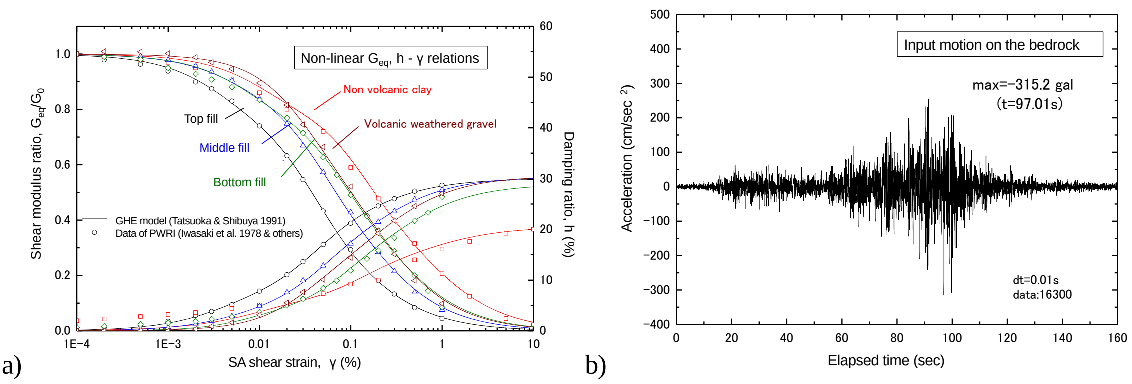

Figure 35. a) Non-linear stress-strain properties used in the equivalent-linear seismic response analysis of old Fujinuma main dam; and b) in-ground acceleration on the bedrock.

4.1.2 *Residual slip displacement by Newmark-D method for actual seismic motion*

To obtain the initial stresses and the cyclic shear stresses by the earthquake motion, static stress analysis and equivalent linear dynamic response analysis were performed by using a FEM model shown in Figure 34, the soil models listed in Table 5 and shown in Figure 34a and the time history of input base horizontal acceleration shown in Figure 34b were used. The input motion was given at the top of the bedrock (having a shear wave velocity V_s equal to 450 m/sec). The base input motion was obtained by a seismic response analysis of the free field ground using the time history of ground acceleration recorded during the 2011 Great East Japan Earthquake at Naganuma, 3 km NW from Fujinuma dam site, (FKSH08). To simulate the energy dissipation through the model boundary, a set of damper was set at the bottom boundary of the model.

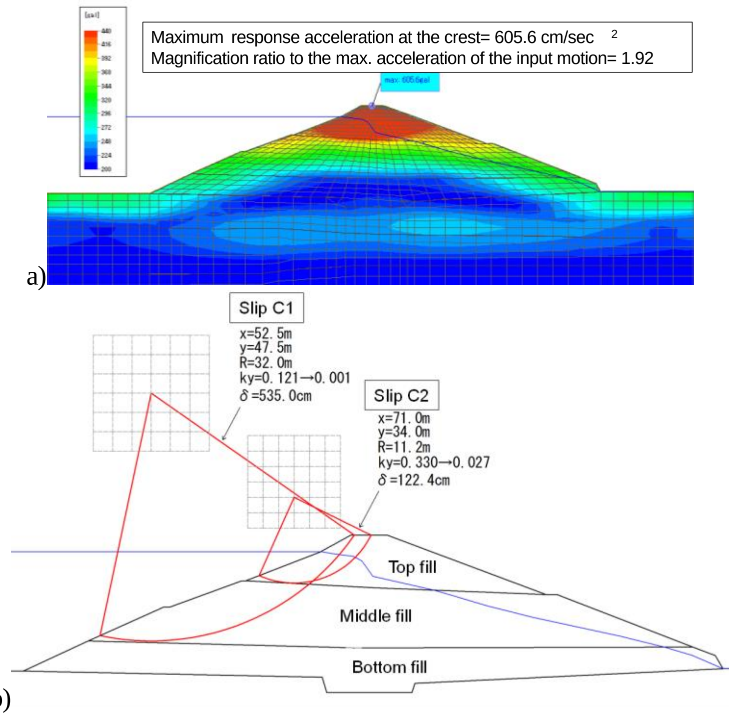

Figure 36: Response of old Fujinuma main dam against the ‘actual’ seismic motion: a) contours of maximum response acceleration by equivalent linear response analysis; and b) two critical slip circles by Newmark-D method.

Figure 36a shows the contours of maximum response acceleration obtained by equivalent linear response analysis. From the results from the earthquake response analysis, the time history of cyclic stresses in each FEM element of the old Fujinuma dam model (Fig. 34) were obtained. Then, the time history of undrained shear strength was obtained using the soil properties data presented in the precedent session by the method explained in the companion paper (Duttine et al. 2016). The global undrained safety factor was obtained by the following equation. This F_s value decreases with time during the whole time history of seismic loading.

$$F_s = \mathrm{Min.}\left[\frac{\sum[\text{transient undrained shear strength}]_i}{\sum[\text{transient peak working shear strength}]_i}\right] \qquad (3)$$

The value of k_h by which the F_s value by Equation 3 becomes unity is defined as the yield horizontal seismic coefficient, k_{hy}. The k_{hy} value continuously decreases with time during a given seismic loading history. Figure 36b shows two critical slip circles along which similar large displacements take place among all possible circular slip planes obtained by the Newmark-D method.

Slip C1, along which the largest slip displacement takes place, is located in both top and middle fills. Slip C2, along which the second largest slip displacement takes place, is located only in the top fill. By comparing Figures 36b with Figure 5, it may be seen that these circular slip planes obtained by this analysis are very similar to the actual ones shown in Figure 5. It is important that these two major slip failures in the actual event are captured by this analysis. With slip C1, the value of k_{hy} decreases from an initial value equal to 0.121 toward a final value equal to 0.001. With slip C2, the value of k_{hy} decreases from an initial value equal to 0.330 toward a final value equal to 0.027. Note that the initial undrained values of k_{hy} (0.121 and 0.330) by these analysis based on Equation 3 is much higher than the drained value based on Equation 1 (0.08, Fig. 33) 172). This is due largely to that the drained shear strength decreases by the action of k_h in Eq. 1, while it does not take place with undrained shear strength in Eq. 3. It is to be noted that these initial undrained values of k_{hy} are relevant to the undrained behavior during a seismic loading, while a drained value equal to 0.08 is not. Such a decrease in the undrained value of k_{hy} as shown above during a given seismic loading substantially increases the ultimate residual slip displacement when compared to the values in which k_{hy} is kept to the initial value. Figure 37 shows the time histories of slip displacement along these two critical circular slip plane by the 'actual' seismic loading obtained by the Newmark-D method. It may be seen that large slip displacements observed in the actual event are well simulated by this analysis. It may be also seen from Figure 37 that, in the analysis, slip C1 and slip C2 start developing nearly simultaneously. On the other hand, it is very likely that, in the actual collapse event, slip C2 started developing earlier than slip C1. It seems that the current analysis method is not accurate enough to capture this sequence of slip occurrence.

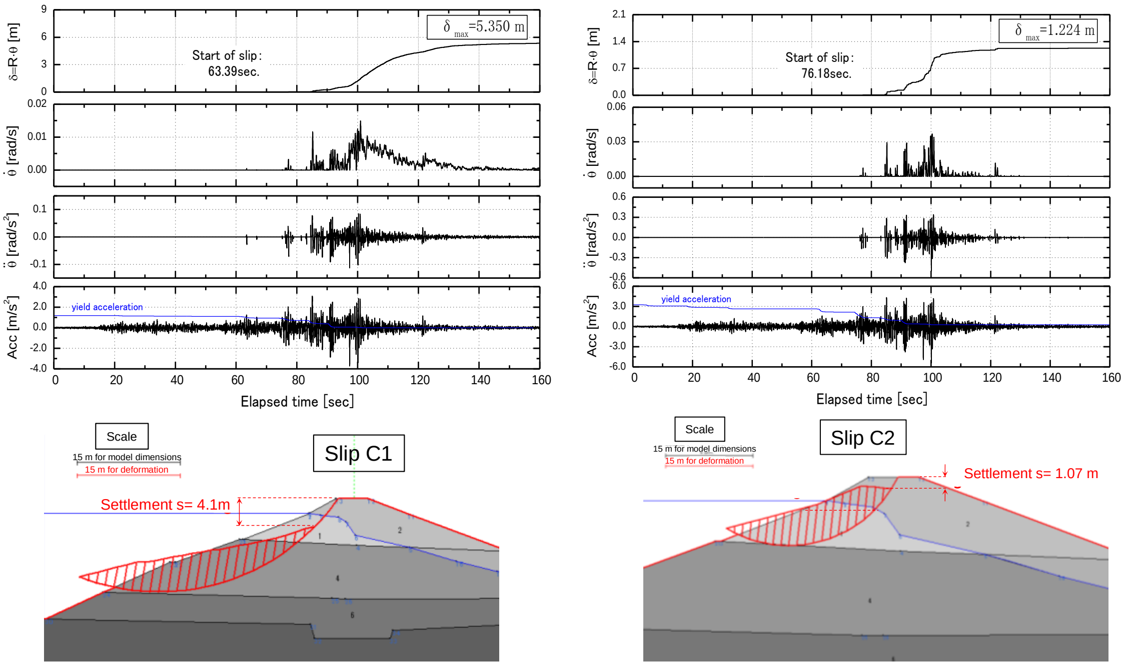

Figure 37. Time histories of slip displacements along two critical slip circles, slips C1 and C2, of old Fujinuma main dam when subjected to 'actual' seismic loading obtained by Newmark-D method.

4.1.3 *Residual deformation by pseudo-static FEM analysis for actual seismic motion*

Figure 38a shows the time history of maximum settlement at the crest at selected peak seismic load states obtained by the pseudo-static non-linear FEM analysis. Figure 38b shows the distribution of evaluated damage strain (in terms of maximum ε_1) in the old main dam. From these damage strains, the transient undrained shear strength in each element is obtained. This figure also shows the maximum displacements at two selected points. These deformations shown in these figures were obtained by subtracting "the initial deformation caused by the gravitational force calculated by the pseudo-static FEM using the initial stress – strain relation" from "the peak deformation at the respective peak seismic load states caused by the gravitational force and the seismic loads calculated by using the transient monotonic stress – strain relations that have deteriorated by preceding cyclic undrained loading”. If any slip displacement does not take place during the whole of a given seismic motion, the displacement at t= 100.14 sec is considered to be the ultimate residual deformation of the dam.

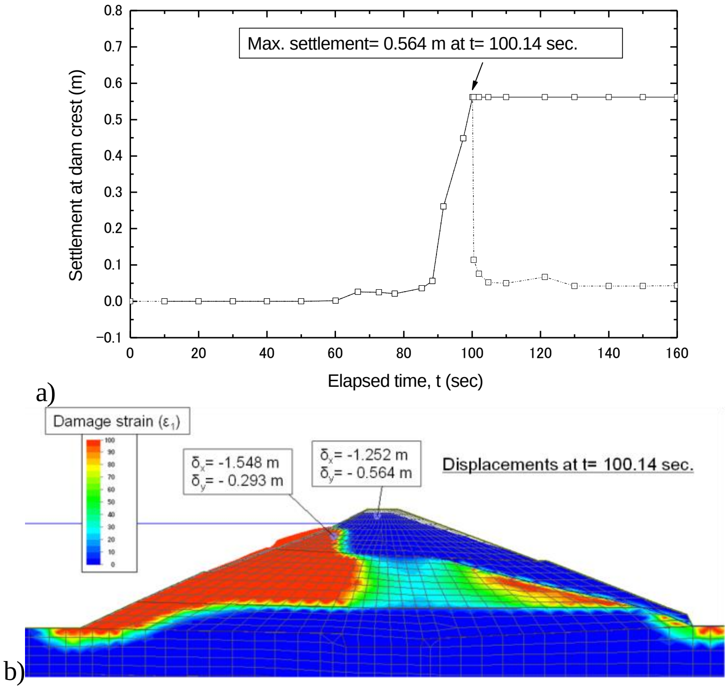

Figure 38: a) Time history of peak settlement at the crest at peak seismic loads; and b) distribution of estimated damage strain (in terms of maximum ε_1) and the maximum displacements at two selected locations of the old main dam, pseudo-static non-linear FEM analysis.

4.1.4 *Total ultimate residual deformation by actual seismic motion*

The ultimate residual deformation of a given slope consists of the following two components:

a) ultimate slip displacements along a circular slip plane (or planes) evaluated by the Newmark-D method; and

b) residual deformation of the slope obtained by removing the deformation due to slip dis placement from the relevant residual deformation obtained by pseudo-static FEM analysis.

The peak deformation calculated at the peak seismic load state after the start of slip displacement obtained by the pseudo-static FEM includes component a). If component a) is properly and fully simulated by the pseudo-static FEM analysis that is employed in this study, this analysis is sufficient to obtain the total ultimate residual deformation, but the analysis by the Newmark-D method becomes unnecessary. However, it is not the case, because component a) takes place forming discontinuous strain fields associated with the development of shear band, while this pseudo-static FEM analysis is not able to properly simulate this phenomenon.

In view of the above, in this analysis, the total ultimate residual deformation was obtained by summing up the following three components:

1) the ultimate slip displacement at the end of seismic loading that is obtained by the Newmark-D analysis (i.e. component a) explained above); and

2) the residual deformation obtained by the pseudo-static FEM analysis that is obtained by summing up the following two sub-components:

2a) the maximum deformation at the peak seismic load state that has taken place in the whole zone by the moment when slip deformation starts according to the Newmark-D analysis; and

2b) the increment of the deformation at the peak seismic load state that has taken place only in the zone below the critical circular slip plane after the start of slip displacement.

By this simplified method, the ultimate residual deformation by slip displacements can be removed from the residual deformation calculated by the pseudo-static non-linear FEM analysis.

Figure 39a shows the total ultimate residual deformation of the old main dam subjected to the 'actual' seismic loading when only global slip C1 takes place in the top and middle fills, obtained by the method described above. Figure 39b shows similar results when only slip C2 takes place locally in top fill. In actuality, both slides C1 and C2 took place. The approximated simulated value of the total ultimate residual settlement at the crest in this case can be obtained by adding the settlement only by slip C2 (= 1.07 m, Fig. 37) to the total ultimate settlement by slip displacement and continuous deformation when only slip C1 takes place (= 4.4 m, Fig. 39a), which results in 5.57 m. This large total settlement at the crest can explain the actual event in which over-topping flow took place and this resulted into the breaching of the main dam.

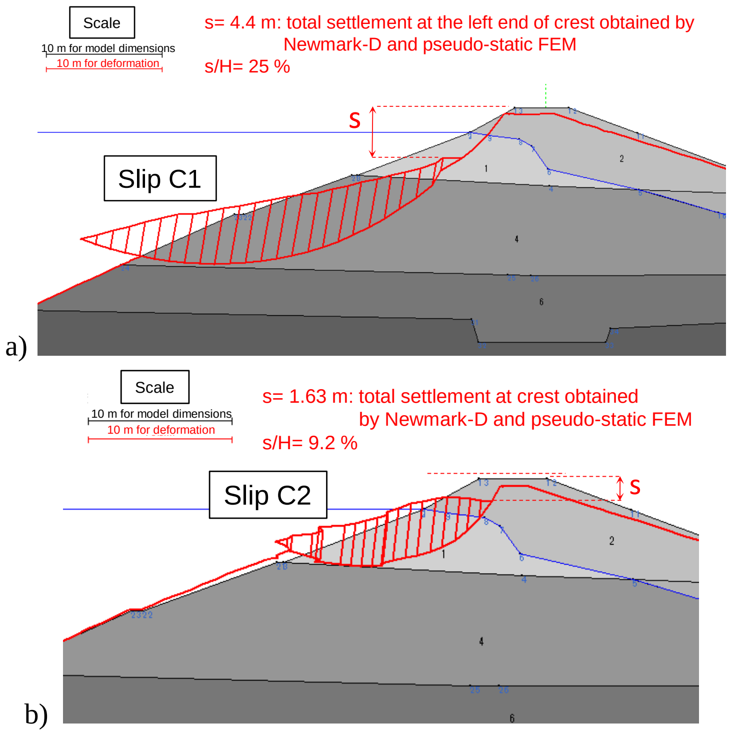

Figure 39: Total ultimate residual deformation of old Fujinuma main dam when subjected to actual seismic loading obtained by summing the deformation evaluated by Newmark-D method and pseudo-static FEM analysis: a) when only a global slip circle in both top and middle fills takes place; and b) when only a local slip circle takes place in top fill.

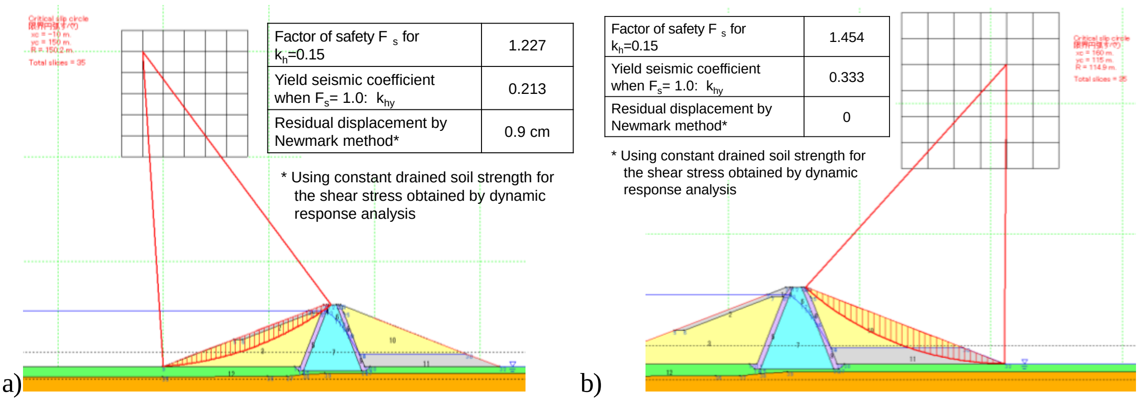

Figure 40. Drained stability against Level 1 design seismic load by Equation 1: a) upstream slope; and b) downstream slope of new Fujinuma main dam.

4.2 *New main dam*

4.2.1 *Safety factor for Level 1 design seismic load*

Figure 40 shows the drained stability against Level 1 design seismic load (i.e., k_h= 0.15) of the upstream and down stream slopes of new Fujinuma main dam, obtained by following the current code. The obtained drained F_s values are substantially higher than the value of the old main dam. Naturally, the downstream slope is more stable than the upstream slope, of which the most zone is unsaturated. The critical failure planes in the upstream and downstream slopes are rather shallow not including slip dispalcemens in the central core zone. This result indicates that, even if these slip failures take place, it will not result in over-topping flow. The residual slip displacement obtained by the Newmark-O analysis using constant drained shear strength against the working shear stress obtained by the earthquake response analysis using the inferred 'actual' seismic load is zero in the downstream slope and very small in the upstream slope.

4.2.2 *Residual slip displacement by Newmark-D method for actual seismic motion*

Static stress analysis and equivalent linear dynamic response analysis were performed by using a FEM model shown in Figure 41, the soil models listed in Table 6 and shown in Figure 42a and the time history of input base horizontal acceleration shown in Figure 34b. Figure 43a shows the contours of maximum response acceleration evaluated by equivalent linear response analysis. Figure 43b shows two critical circular slip planes along which the slip displacement was evaluated by the Newmark-D method. With slip C1, the value of k_{hy} decreases from a high initial value equal to 0.594 toward a high final value equal to 0.541. With slip C2, the value of k_{hy} also decreases from a high initial value equal to 0.728 toward a high final value equal to 0.677. Therefore, no slip displacement took place along these slip planes (Fig. 44). The initial undrained values of k_{hy} obtained based on Equation 3 (0.541 & 0.728) are much higher than the drained value obtained based on Equation 1 (0.213, Fig. 40a). This is due largely to that: a) the drained shear strength decreases by the action of k_h in Eq. 1, while it does not take place with undrained shear strength in Eq. 3; and b), as seen from Figures 28 and 29, the undrained shear strength is much larger than the drained peak strength at the effective confining pressure equal to the initial value because of good compaction. This result indicates that the new main dam is much more stable than the old main dam while exhibiting a very high stability even when subjected to Level 2 seismic loading.

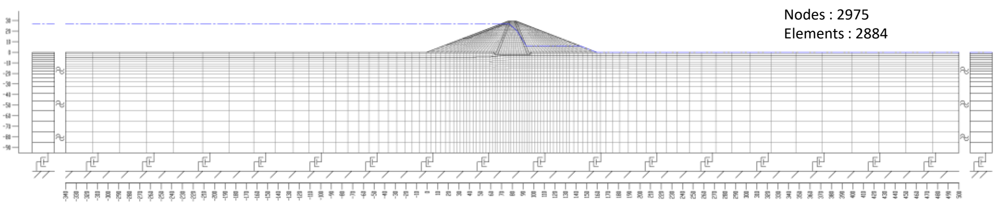

Figure 41. FEM model for static stress analysis, equivalent-linear seismic response analysis and pseudo-static residual deformation analysis of new Fujinuma main dam.

Table 6. Soil models for static stress analysis, equivalent-linear seismic response analysis of new Fujinuma main dam.

		γ_t (kN/m^3)	γ_{sat} (kN/m^3)	For static stress analysis		For dynamic response analysis		
				E (MPa)	ν	G_0 (MPa)	ν	G-h-γ properties
①	Shell	21.1	21.3	6	0.45	290※1	0.45	By cyclic triaxial tests
②	Core	20.3	20.8	23	0.45	138※1	0.45	By cyclic triaxial tests
③	Rock※3	20.5	23.0	40	0.35	350	0.35	same as shell
④	Filter※4	19.9	22.3	40	0.35	350	0.35	same as core
⑤	Volcanic weathered gravel※6	17.7	17.7	23.0	0.30	150※2	0.441※2	Pleistocene epoch gravel ※5
⑥	Volcanic weathered granite※6	19.6	19.6	143.0	0.30	380※2	0.449※2	Constant h=2.0%

※1 by cyclic triaxial tests,
※2 based on field shear wave velocity measurements by PS logging
※3,4 parameters based on the properties of typical rock and filter materials used in neighbouring dams
※5 empirical relations from Japan Public Work Research Institute (PWRI, Iwasaki et al. 1978 & others)
※6 Early Pleistocene epoch in Quaternary period, Shirakawa stratum

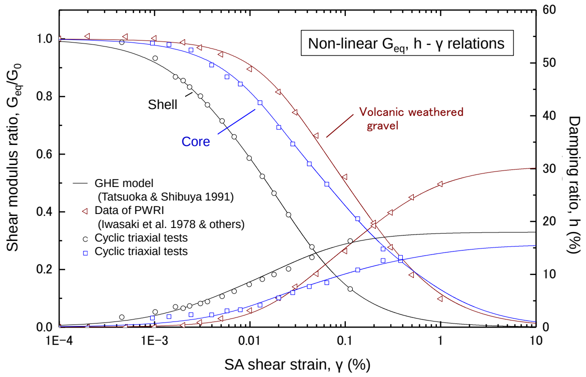

Figure 42. Non-linear stress-strain properties used in the equivalent-linear seismic response analysis of new Fujinuma main dam.

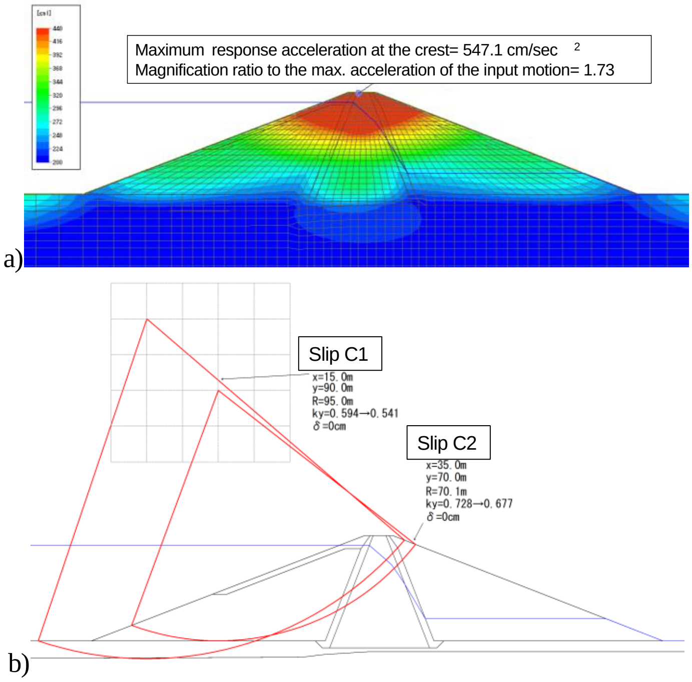

Figure 43: Response of new Fujinuma main dam against the actual seismic loading: a) contours of maxi mum response acceleration by equivalent linear response analysis; and two critical circular slip planes by Newmark-D method.

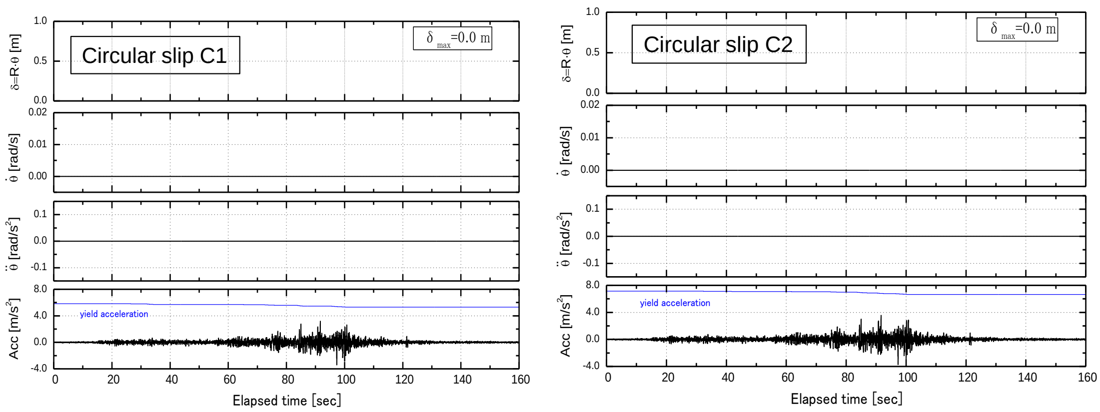

Figure 44. Time histories of slip displacements along two critical circular slip planes in the upstream slope of new Fujinuma main dam when subjected to ‘actual’ seismic loading by Newmark-D method.

4.2.3 *Residual deformation by pseudo-static non-lnear FEM analysis for actual seismic motion*
Figure 45a shows the time history of the peak settlement at the crest at selected peak seismic load states obtained by the pseudo-static non-linear FEM analysis. Figure 45b shows the displacements at two locations of the new main dam when the deformation of the dam becomes largest during the 'actual' seismic loading. The corresponding contours of damage strain are also presented. Large residual deformation takes place only in a shallow zone in the upstream slope, indicating that the danger of over-topping flow is very low.

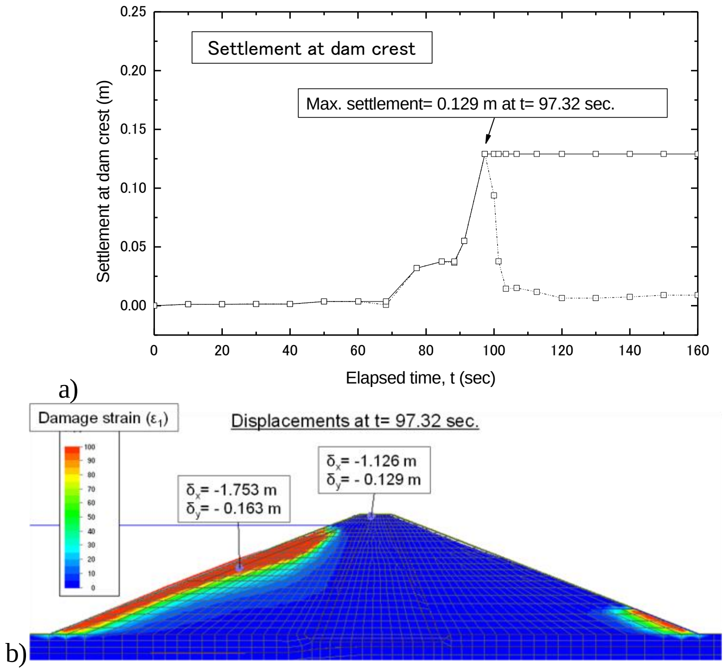

Figure 45. a) Time history of maximum settlement at the crest observed at peak seismic load states; and b) distribution of estimated damage strain (in terms of maximum value of ε_1) in the new main dam and the maximum displacements at two selected points, pseudo-static non-linear FEM analysis.

4.2.4 *Total ultimate residual deformation for actual seismic motion*
Figure 46 shows the total ultimate residual deformation of the new main dam subjected to 'actual' seismic loading obtained by the method described above. The estimated total residual settlement at the crest is only 0.129 m, which is acceptable as the performance when subjected to Level 2 seismic load at this site. The seismic stability analysis of the new main dam based on the soil properties at actual compacted states will be performed later.

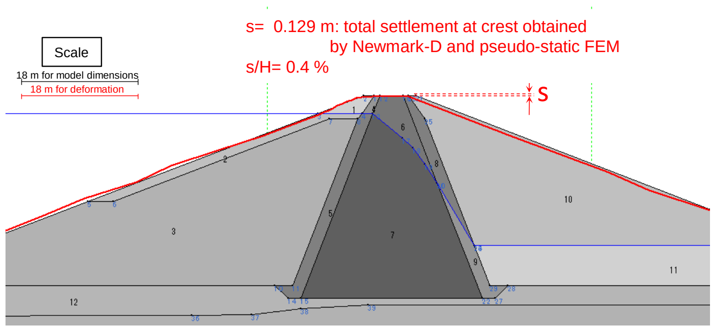

Figure 46. Total ultimate residual deformation of the dam of new Fujinuma main dam when subjected to actual seismic loading obtained by summing the deformation evaluated by Newmark-D method and pseudo-static FEM analysis.

5 CONCLUDING REMARKS

It is reported that the main and auxiliary Fujinuma dams collapsed by the 2011 Great East Japan Earthquake and they are now being restored to much more stable ones (August 2016). They will be completed by April 2017. The following conclusions were obtained:

1) The soil types and compacted dry densities of the collapsed two dam inferred from the measurements in limited zones that survived the earthquake showed that: a) the compacted state was generally poor; and b) the top fill consisted of particularly poorly compacted sandy soil, which would have resulted in a significant reduction of undrained strength by cyclic undrained loading and a fast erosion by over-topping flow. A prolonged strong seismic motion is an addition factor among the major causes for the collapse.

2) A series of monotonic undrained loading triaxial tests were performed before and after application of cyclic undrained cyclic loading with different magnitudes on saturated specimens of the backfill materials retrieved from the collapsed main dam. The specimens were compacted to different dry densities. Similar data of better compacted backfill materials of higher quality were obtained at the design stage of the new dams. These data sets were summarized in a single framework so that they can be used in the simulation of the collapse of the old main dam and in the stability analysis of the new dams by “slip displacement analysis by the Newmark-D method” and “residual deformation analysis by the pseudo-static FEM”, both taking into account the seismic forces. These analyses incorporate the continuous degradation of the stress-strain properties by cyclic undrained loading.

3) The collapse of the old main dam could be very well simulated by the analysis described above. We can conclude based on the stability analysis by the same methods as above that the new dams are much more stable due to much better compaction and the use of better controlled soil types.

4) The results of the compaction control at the early stage of the restoration work for the new dams show that the newly proposed method that controls the water content of the backfill to be compacted and the dry density and the degree of saturation of compacted soil works very well to efficiently achieve high dry density states realizing high shear strength, low hydraulic conductivity and small collapse and small strength reduction upon wetting.

REFERENCES

Duttine, A., Tatsuoka, F., Shinbo, T. and Mohri, Y. 2016: A new simplified seismic stability analysis taking into account degradation of soil undrained stress – strain properties and effects of compaction, *Proc. International Symposium on Qualification of dynamic analyses of dams and their equipment and of probabilistic assessment of seismic hazard in Europe, 31th August – 2nd September, Saint-Malo, France* (this symposium) (eds. Fry, J.-J. and Matsumoto, N.).

Santanbata, I., Nagai, H., Yamagishi, A., Tatsuoka, F., Nakayama, M., Miura, T. and Watanabe, H. 2016: Control of the degree of compaction in construction of Fujinuma Dam (No. 1: outline of the embankment management), *Proc. 51th Japan National Conference on Geotechnical Engineering,* Paper No. 599, 999-1000 (in Japanese).

Iwasaki,T., Tatsuoka,F. and Takagi,Y. (1978), “Shear moduli of sands under cyclic torsional loading”, *Soils and Foundations*, Vol.18, No.1, 39-56.

Ministry of Agriculture, Forestry and Fisheries 2006: Planning and design criteria of land improvement project “earth dam”, Design code, February 2006. (in Japanese)

International Symposium on Qualification of dynamic analyses of dams and their equipment and of probabilistic assessment of seismic hazard in Europe, 31th August – 2nd September, Saint-Malo, France (this symposium) (eds. Fry, J.-J. and Matsumoto, N.)

Ministry of Agriculture, Forestry and Fisheries 2015: Planning and design criteria of land improvement project "earth dam", Design code, May 2015 (in Japanese).

Nagai, H., Santanbata, I., Yamagishi, A., Tatsuoka, F., Nakayama, M., Miura, T. and Watanabe, H. 2016: Control of the degree of compaction in construction of Fujinuma Dam (No. 1: results), *Proc. 51th Japan National Conference on Geotechnical Engineering,* Paper No. 600, 1001-1002 (in Japanese).

Pradhan, Tej B.S., Tatsuoka,F. and Sato,Y. 1988: Undrained stress strain behavior of sand subjected to earthquake wave loading", *Proc. of the 9th World Conference on Earthquake Engineering,* Vol.3, 267-272.

Proctor, R. R. 1933: Fundamental principles of soil compaction, *Engineering News-Record*, *New York*, Vol.111, No.9, August 31, 55-58.

Tanaka, T., Tatsuoka, F., Mohri, Y. 2012: Earthquake Induced Failure of Fujinuma Dam, *Proc. Int. Symp. on Dams for a Changing World, Kyoto*, June 5, Vol. 6, 47-52.

Tatsuoka, F. and Shibuya, S. 1991: Deformation characteristics of soils and rocks from field and laboratory tests", Keynote Lecture for Session No.1, *Proc. of the 9th Asian Regional Conf. on SMFE,* Bangkok, Vol.II, 101-170.

Tatsuoka, F. 2016: Stress-strain behaviour of compacted soils related to seismic earth-fill dam stability, *Proc. International Symposium on Qualification of dynamic analyses of dams and their equipment and of probabilistic assessment of seismic hazard in Europe, 31th August – 2nd September, Saint-Malo, France* (this symposium) (eds. Fry, J.-J. and Matsumoto, N.).

Ueno, K., Mohri, Y., Tanaka, T. and Tatsuoka, F. 2013: Strength reduction due to cyclic undrained loading of irrigation dam materials, *Proc. 48th Japan National Conference on Geotechnical Engineering, Toyama,* 1201-1202.

Ueno, K., Mohri, Y., Tanaka, T. and Tatsuoka, F. 2014: Effects of compaction degree on the strength reduction rate by cyclic undrained loading of saturated soil, *Proc. 49th Japan National Conference on Geotechnical Engineering, Kitakyushu*, 1395-1396.

Japanese Society for Civil Engineers 1996: Second recommendations about the seismic design standards for civil engineering structures, 10 January 1996 (in Japanese).